ORIGINAL PAPER

Footprints of element mobility during metasomatism linked to a late Miocene peraluminous granite intruding a carbonate host (Campiglia Marittima, Tuscany)

Gabriele Paoli[1] · Andrea Dini[2] · Sergio Rocchi[1]

Abstract

The Campiglia Marittima magmatic-hydrothermal system includes a peraluminous granite, its carbonatic host, and skarn. The system evolved generating a time-transgressive exchange of major and trace elements between granite, metasomatic fluids, and host rock. The process resulted in partial metasomatic replacement of the granite and severe replacement of the carbonate host rocks. The fluid activity started during a late-magmatic stage, followed by a potassic–calcic metasomatism, ending with a lower temperature acidic metasomatism. During the late-magmatic stage, B-rich residual fluids led to the formation of disseminated tourmaline–quartz orbicules. High-temperature metasomatic fluids generated a pervasive potassic–calcic metasomatism of the granite, with replacement of plagioclase, biotite, ilmenite, and apatite by K-feldspar, phlogopite–chlorite–titanite, titanite–rutile, and significant mobilization of Fe, Na, P, Ti, and minor HFSE/REE. The metasomatized granite is enriched in Mg, K, Rb, Ba, and Sr, and depleted in Fe and Na. Ca metasomatism is characterized by crystallization of a variety of calc-silicates, focusing along joints into the granite (endoskarn) and at the marble/pluton contact (exoskarn), and exchange of HFSE and LREE with hydrothermal fluids. Upon cooling, fluids became more acidic and fluorine activity increased, with widespread crystallization of fluorite from disequilibrium of former calc-silicates. At the pluton-host boundary, fluids were accumulated, and pH buffered to low values as temperature decreased, leading to the formation of a metasomatic front triggering the increasing mobilization of REE and HFSE and the late crystallization of REE–HFSE minerals.

Keywords Magmatic-hydrothermal system · Fluid–rock interaction · Element mobility · Acidic metasomatism

Introduction

Metasomatic rocks occur in all continents and are hosted in rocks of every type and age, yet they are most commonly found within or near carbonate rocks spatially associated with magmatic bodies. In the simplest scenario, these deposits form by the transfer of heat, fluids, and metals from a cooling magma to the surrounding rocks, leading also to

✉ Gabriele Paoli
gabrielepaoli88@gmail.com

1 Dipartimento di Scienze della Terra, Università di Pisa, Via Santa Maria 53, 56126 Pisa, Italy

2 CNR, Istituto di Geoscienze e Georisorse, Via Moruzzi 1, 56124 Pisa, Italy

hydrothermal alteration (*skarn*—Meinert et al. 2005). Metasomatic-hydrothermal alteration is a complex process involving textural, mineralogical, and chemical changes, resulting from the interaction of hot aqueous fluids with the rocks through which they circulate, under evolving physico-chemical conditions. Intense circulation of fluids released by an igneous intrusion commonly occurs in contact aureoles (Harlov and Austrheim 2013; Pirajno 2009). Outline geometries and spatial relationships among the main geological bodies, as well as rock textures, mineral paragenesis, and mineral zoning are relevant to reconstruct the hydrothermal fluid paths and shed light on the processes of fluid–rock interaction and element mobility in a magmatic-hydrothermal system (e.g., Pirajno 2009, 2013; Harlov and Austrheim 2013). As an example, when hydrothermal fluids are channeled out of a granite in a carbonate-rich rock, mineral-fluid equilibria become much more complex due to the reactive nature of the host rock, generating a wide variety

of skarn-replacement deposits at the pluton–host boundary (Einaudi et al. 1981).

The magmatic-hydrothermal system of Campiglia Marittima, Tuscany, Italy, has received much attention from mineralogists and petrologists during the past decades, mostly because it is characterized by multiple igneous bodies accompanied by multi-stage hydrothermal products (Vezzoni et al. 2016 and references therein). The main intrusion (*Botro ai Marmi monzogranite*) generated contact metamorphism and synchronous deformation of the carbonate host rock (Vezzoni et al. 2018). At the pluton/marble contact, exoskarn occurs as either massive bodies crosscutting the contact metamorphic foliation, or selective replacement of the ductilely folded layers of the host rock. On the other side, calc-silicate endoskarn bodies follow joints in the granite pluton connected with the contact exoskarn.

The previous works focused on the identification of the wealth of new minerals found at the Botro ai Marmi mine site, as well as on the mineralogy of the limestones and the associated metasomatic products (*skarn*) recognized at Botro ai Marmi (Barberi et al. 1967; Leoni and Tamponi 1991; Biagioni et al. 2013). In contrast, this work investigates in detail the spatial, textural, and genetic relationships of the metasomatic mineral assemblages at the pluton–marble contact. The present study was undertaken to obtain detailed information on these features and relationships: their knowledge is crucial to understand how elements are mobilized by hydrothermal fluids between magmatic, metasomatic, and metamorphic rocks in a magmatic-hydrothermal system. Specific rock-forming processes and their physical conditions are also pivotal to support ongoing petrochronology studies. Consequently, this paper is based on a detailed textural, mineralogical, and geochemical description of the monzogranite, the host carbonate rocks, and metasomatic products, which has been carried out in the field, under the optical microscope and by QEMSCAN (Quantitative Evaluation of Minerals by SCANning Electron Microscopy), EPMA (Electron probe micro-analysis), and (LA)-ICP-MS (Laser-ablation Inductively coupled Plasma Mass Spectrometry).

Geological framework

The Campiglia area is characterized by an N–S oriented Mesozoic carbonate horst, mainly represented by the carbonatic sequence of the Tuscan Nappe (Fig. 1; Vezzoni et al. 2016). The horst, developed in the inner part of the Apennine thrust-and-fold belt as a consequence of Miocene to Recent post-collisional extensional tectonics, is bounded by high-angle extensional and strike-slip faults (Acocella et al. 2000; Rossetti et al. 2000; Vezzoni et al. 2018). Extension produced thinning of the crust (~ 22 km), widespread

magmatism involving both crustal anatectic and mantle-derived products, and diffuse hydrothermal–metasomatic activity, generating the Campiglia Marittima igneous-hydrothermal complex (Barberi et al. 1967; Dini et al. 2005; Vezzoni et al. 2016).

The magmatic activity of this complex started during the late Miocene (~ 5.44 Ma; Paoli et al. 2017; Paoli 2018), when the Campiglia carbonate horst was intruded by the Botro ai Marmi peraluminous monzogranite pluton (Fig. 1), cropping out where the top of a bulge is quarried in the open-pit mine of Botro ai Marmi (~ 0.25 km^2). Drilling logs, which document occurrence of the pluton at Monte Spinosa and Monte Valerio, 3 km south of the outcrop, along with geophysical data, are evidence for a larger size of the pluton with N–S elongation (Fig. 1). The pluton is characterized by a length/width ratio of 3–6, an E–W strongly asymmetric profile over an area of about 18 km^2 (Vezzoni et al. 2018). The magma was emplaced at a depth corresponding to ca. 0.10–0.15 GPa (Leoni and Tamponi 1991), producing a thermal aureole in the host rock, with temperatures as high as 500–550 °C at the contact. The previous studies (Barberi et al. 1967; Caiozzi et al. 1998; Lattanzi et al. 2001; Rodolico 1945) described the main pluton as a monzogranite, consisting of quartz, K-feldspar, plagioclase, and biotite, along with accessory minerals and late-stage tourmaline.

The large contact metamorphic aureole is pervasively deformed, with foliation parallel to the intrusive contact and defining a broad antiform with an NE–SW to N–S axial plane mimicking the shape of the pluton bulge (Fig. 1; Vezzoni et al. 2018). Minor, irregular exoskarn masses occur at the pluton–carbonate host contact and as aligned bodies into the host rock, while endoskarn bodies are observed inside the monzogranite body. Much more voluminous skarn, associated with Fe–Cu–Zn–Pb(–Ag) deposits, are found a few km E–NE of the pluton outcrop and ~ 1 km above the pluton roof in the contact metamorphic white marble (Vezzoni et al. 2016). These skarns are crosscut by both mafic and felsic porphyritic dykes, all affected by potassic alteration (Vezzoni et al. 2016). A significant Sn deposit is found at Monte Valerio, 3 km south of the granite outcrop. The closing magmatic–metasomatic event is constrained by the emplacement of the felsic porphyritic dykes (whole-rock K–Ar age of 4.30 ± 0.13 Ma; Borsi et al. 1967) and by the San Vincenzo rhyolite igneous episode (sanidine ^{40}Ar–^{39}Ar age of 4.38 ± 0.04 Ma; Feldstein et al. 1994).

Analytical methods

Samples were collected from the uppermost, central, and lowermost levels of the outcropping granite, as well as the overlying marble (Fig. 1). Mineral investigations (by scanning electron microscopy and analyses by energy dispersive
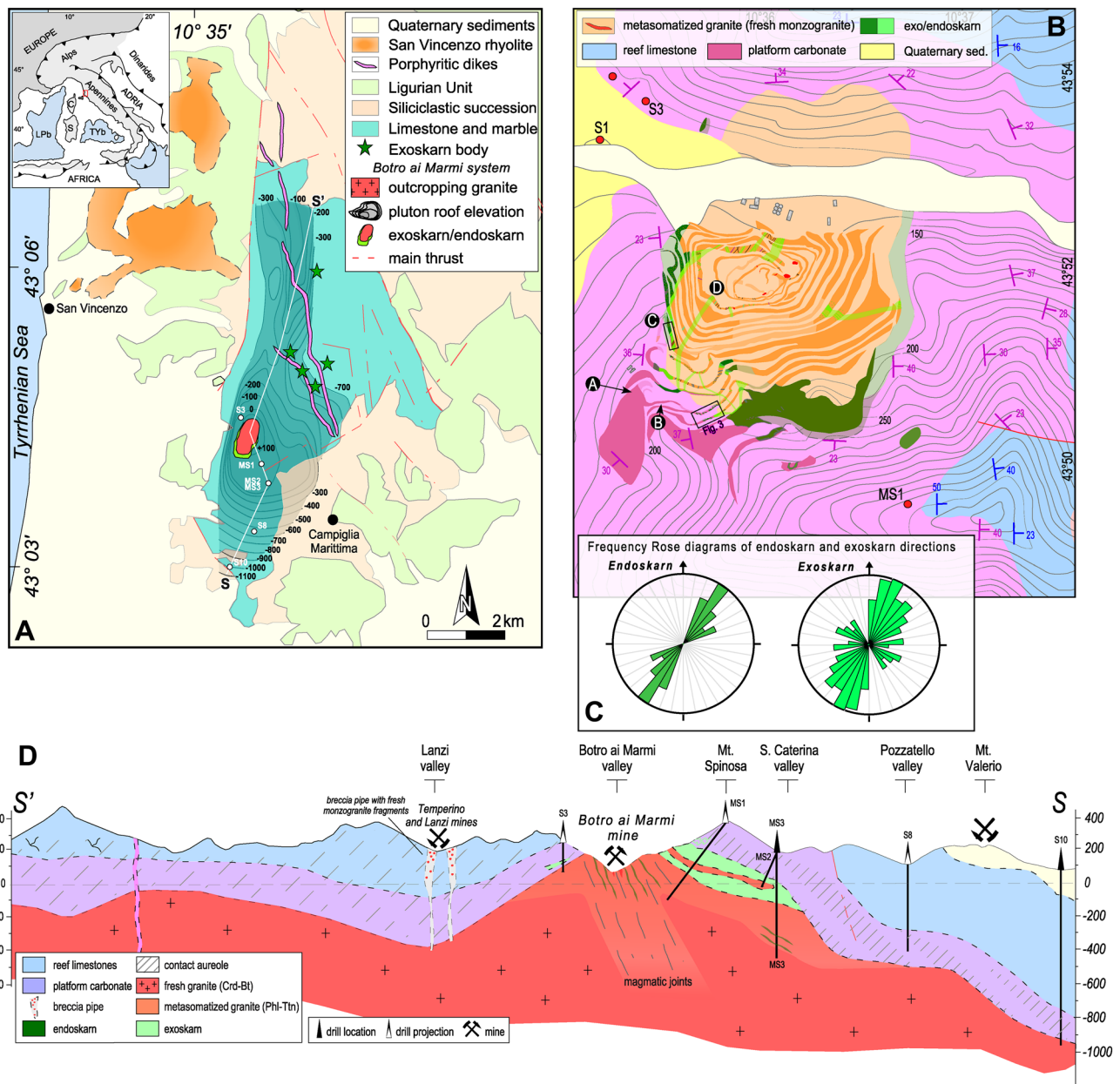
Fig. 1 **a** Morphologies of the contact between the Botro ai Marmi pluton and the limestone/marble host, as reconstructed by means of the schematic geological map of the Campiglia Marittima area, and the interpretive map showing the pluton roof reconstructed by borehole log and geophysical data (modified after Vezzoni et al. 2016). Note the asymmetric pluton roof morphology with an elevation maximum in the Botro ai Marmi outcrop. Furthermore, the host rocks show a strong thickness variation, progressively thicken away from the mine and from southern to eastern side (Vezzoni et al. 2016). **b** Geologic map of the Botro ai Marmi mine (full colors indicate lithologies in outcrop; faint colors indicated inferred lithologies). **c** Length proportional to frequency rose diagrams show the directions of the outcropping endoskarn and exoskarn bodies (for method details, see Dini et al. 2008). Note the asymmetric pluton roof morphology with a maximum in the Botro ai Marmi outcrop. **d** Interpretive section showing lithological distribution with depth and the location of drill core (modified after Dini et al. 2013)

system—SEM–EDS), and major (via X-ray fluorescence—XRF) and trace element (by inductively coupled plasma mass spectrometry—ICP-MS) analyses, as well as porosity and density measurement were performed at the Earth Science Department, University of Pisa. Automated mineral analysis and textural imaging were performed using an FEI QEMSCAN Quanta 650F facility at the Earth Sciences Department, Geneva University. Mineral chemistry was performed at University of Milano, using an electron microprobe (EPMA) equipped with five wavelength-dispersive

spectrometers and an EDS detector. Detailed analytical methods are reported in Supplementary Materials.

Results: petrographic features of the Botro ai Marmi magmatic-hydrothermal system

At Botro ai Marmi, the exposed lithologies can be distinguished as: (1) cordierite–biotite monzogranite (Crd–Bt granite), showing a typical grayish color, found only as scattered relict patches along an NE–SW-trending zone (Fig. 1); (2) its metasomatized counterpart, a pinkish–whitish, phlogopite–titanite monzogranite (Phl–Ttn granite): it covers more than 95% of the pit exposure, and it is the most represented lithology down to ~ 400 m (see MS3 borehole description); (3) a greenish endoskarn occurring with sharp borders along brittle magmatic joints crosscutting the granite with NE–SW to E–W sub-vertical attitude, and characterized by a complete textural rearrangement (Figs. 1, 2); (4) several exoskarn lithotypes linked to the pluton–marble contact (Fig. 2), and reflecting the original limestone–marly limestone alternation; (5) the host carbonate rock.

A full petrographic description of rock samples from both the outcrop and available drill cores is presented, underlining the differences between mineralogical paragenesis (Table 1). In this work, endoskarn and exoskarn are used as lithologic terms and do not strictly refer to their genetic evolution, although endoskarn actually replaces igneous rocks and exoskarn replaces host rock. Abbreviations for mineral names are used according to Whitney and Evans (2010).

Botro ai Marmi mine

Evaluation of the mineral paragenesis is based on field and petrographic observations, and SEM–EDS investigations. Textural relationships are clearly magmatic (Figs. 3, 4), with phenocrysts of K-feldspar occurring as isolated relict crystals displaying dissolution textures (Fig. 3f). Metasomatic minerals were recognized on the basis of replacement and dissolution/precipitation textures and their occurrence in veins (Fig. 4a, e, g). Both the monzogranite and the marble are extensively metasomatized and replaced by metasomatic calc-silicates (e.g., diopside, vesuvianite, garnet, titanite, and epidote), phlogopite, REE-rich accessory minerals (e.g., allanite and apatite) and sulfides (Figs. 3, 4).

Host carbonate rock The intense metamorphism of the carbonate sequence (~ 8 km^2 metamorphic aureole; Vezzoni et al. 2018) generated a medium/coarse-grained white–pink marble with grey streaks (Figs. 1, 2). Metamorphic paragenesis includes calcite and dolomite, as well as minor quartz, phyllosilicates (Ms and Phl), and Cu–Fe–Pb–Zn sulfides. Marble shows some disequilibrium evidence with a granoblastic sutured texture, typical of quick recrystallization of carbonates under HT–LP contact metamorphism.

Metamorphic temperatures between 550 and 430 °C are obtained using the calcite–dolomite geothermometer (Franzini et al. 2010). Lobate to sutured grain boundaries as well as tabular phlogopite crystals grown along calcite grain boundaries point to highly interconnected porosity (Franzini et al. 2010).

Cordierite–biotite granite Cordierite–biotite granite is found as few small patches inside the Botro ai Marmi mine, in deep portions of monzogranite brought at shallow depth by breccia pipes (Temperino mine, Fig. 1), and, moving to the south, at increasing depth in several boreholes (MS1 = 550 m, MS3 = 500 m, S10 = 950 m; Fig. 1). The original pluton is a medium-grained, cordierite–biotite granite (Figs. 2, 3), rarely with K-feldspar-phyric texture. The primary igneous assemblage consists of K-feldspar (30–35 vol%), quartz (30–35 vol%), plagioclase (20–30 vol%), and biotite (5–10 vol%), along with accessory cordierite, apatite, zircon, and late-magmatic tourmaline (Table 1; Fig. 3e, f). Cordierite represents the most abundant accessory mineral, indicating the peraluminous character of this rock (Fig. 3l). Tabular K-feldspar (orthoclase, Or$_{85–90}$, $n = 7$) commonly occurs as megacrysts with average size around 1 cm, reaching up to ~ 5–6 cm, and showing rare perthitic exsolution (Fig. 3a–c). Interstitial Kfs is also present. Plagioclase cores (An$_{35–45}$, $n = 11$) are usually slightly zoned with ward albite enrichment (Fig. 3a–c). These cores are commonly characterized by a thin oligoclase overgrowth (An$_{10-15}$). Biotite is the main representative mafic mineral (Fig. 3f). Its composition is annite/siderophyllite, with Fe# values of 0.4–0.6, comparable with other peraluminous magmas from Tuscany such as Monte Capanne pluton (Farina et al. 2010) and San Vincenzo rhyolite (Ridolfi et al. 2016). Major element data for K-feldspar and biotite are reported in Supplementary Tables.

Metasomatic phlogopite-titanite granite The previous studies (Barberi et al. 1967; Caiozzi et al. 1998; Lattanzi et al. 2001; Rodolico 1945) argued that a pervasive hydrothermal alteration had been responsible for elevated K$_2$O contents, up to 6–8 wt%, occurrence of replacement K-feldspar, loss of Ca–Fe–S, and widespread replacement of biotite (Fig. 3). The current study highlights that the metasomatic alteration of the cordierite–biotite granite produced a pinkish–white metasomatized granite, representing 95% of outcropping granite. It is characterized by the almost complete replacement of biotite by phlogopite (Mg# = 0.85–0.95), chlorite, titanite, and Ti oxide. The rare biotite remnants (Fig. 3) are characterized by high contents of FeO (up to 25 wt%) and TiO$_2$ (up to 4 wt%) and diffuse replacement by numerous metasomatic minerals (i.e., chlorite, phlogopite, titanite, fluorite, rutile, and adularia). In close spatial relation with strongly metasomatized biotite, accessory minerals such as apatite, zircon, and minor monazite are commonly recrystallized. Feldspars show peculiar
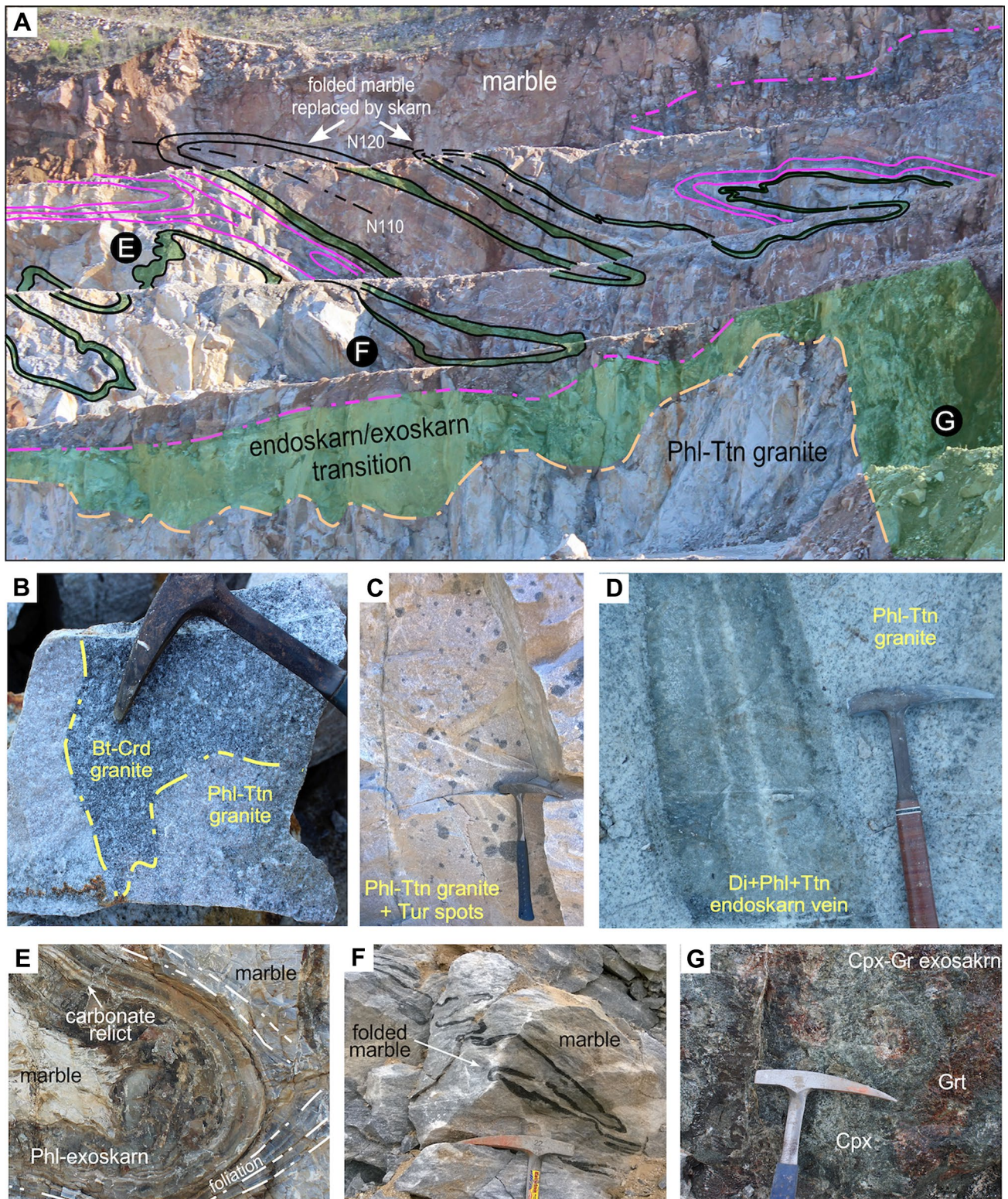
Fig. 2 **a** Panoramic view and deformation structures at the granite–marble contact. Some folds are replaced by exoskarn. **b** Cordierite–biotite vs. metasomatized granite. **c** Metasomatized granite with tourmaline *orbicoles*. **d** Endoskarn bodies. **e** Folded marble replaced by phlogopite–diopside exoskarn, into layered grey marble. The core of the fold shows indented contact. **f** Centimetric folds into white–grey marble. **g** Vesuvianite–garnet exoskarn with calcite veins

Table 1 Modal (vol %) abundance for the main lithotypes sampled at the Botro ai Marmi mine

Mineral paragenesis	Fresh Crd–Bt	Metasomatized	Endoskarn	Exoskarn		
	Monzogranite	Phl–Ttn granite		Di–Ttn–Phl	Phl-rich	Grt > Vs and Vs > Grt
Igneous						
Quartz	30–35	45–50	5-10	< 5	rare	trace
K-feldspar	30–35	25–30	< 5	< 5	< 5	–
Plagioclase (An$_{35-45}$)	5–10	5–10	5–10	5–10	trace	trace
Plagioclase (An$_{10-15}$)	15–20	< 5	< 5	< 5	< 5	
Biotite	5–10	< 1	trace	–	–	–
Tourmaline	< 5	< 5	–	–	–	–
Metasomatic						
Phlogopite	–	5–10	5–10	5–10	30-35	5–10
Titanite	–	1–3	5–10	5–10	5–10	5–10
Diopside	–	–	15–25	25–35	20–25	5–10
Vesuvianite	–	–	trace	< 5	< 5	20–40
Garnet	–	–	trace	< 5	< 5	10–30
Albite	–	–	< 5	< 5	5–10	< 5
Allanite	–	trace	< 5	< 5	< 5	< 5
Calcite	–	trace	5–15	10–20	10–15	< 5
Sericite	< 5	< 5	< 5	–	–	–
Chlorite	<1	1–3	< 5	< 5	< 5	< 5
Sulfides	< 5	< 5	< 5	< 5	< 5	< 5
Accessory minerals	Zrn, Ap, Tur, Mnz, Ttn, Rt	Zrn, Ap, Tur, Rt, Aln, Cal, Fl, Thr, Urn	Zrn, Ap, Rt, Fl, Ep, Thr, Urn	Zrn, Ap, Ep, Fl, Thr, Urn	Ap, Zrn, Ep, Fl	Zrn, Ap, Ep, Fl,
Density (g/cm^3)	2.64	2.66	2.69–2.70	3.34	2.92	3.53

Crd–Bt granite cordierite–biotite granite, *Phl–Ttn granite* metasomatized granite characterized by Phl and Ttn, *Phl–Ttn–Di granite* metasomatized granite characterized by widespread Di–(Phl–Ttn) aggregates

characteristics (Fig. 3g–i). The oligoclase abundance is considerably reduced down to ~ 5 vol % (Table 1; Fig. 3a–c). The rim (*oligoclase*) is almost completely isotropically replaced by irregularly shaped K-feldspar (~ Or$_{80–90}$). Replacement of plagioclase also occurs along polysynthetic twinning and fractures. The progressive replacement of plagioclase (oligoclase) by K-feldspar is directly proportional to the proximity to the endoskarn bodies. There, crystallization of widespread metasomatic diopside, titanite, and accessory minerals took place (Fig. 4). Late calcite usually fills microfractures (Fig. 4e, h). Accessory minerals usually show evident replacement and/or recrystallization textures (Fig. 4g, i): (1) cordierite, typical of Tuscan crustal-derived igneous products (i.e., San Vincenzo and Roccastrada rhyolites, Ferrara et al. 1989), is commonly deeply altered or replaced by pinite and is, therefore, identified from its shape and the composition of its relics (Fig. 3l); (2) ilmenite, another common mineral crystallizing from Tuscan crustal magmas, is usually extensively replaced by titanite and rutile aggregates; crystals up to 100–150 µm, bordering metasomatized biotite, likely represent metasomatic crystals (Fig. 3g); (3) primary monazite (< 50 µm) is strongly affected by metasomatic alteration, showing clear dissolution textures;

unaltered monazite is observed as small, euhedral crystals (5–10 µm) widespread inside interstitial K-feldspar, quartz, or as aggregate with bigger apatite and zircon (Fig. 3h, i); (4) zircon consist of 50–250 µm crystals included in biotite, at odds with respect to small (5–20 µm), euhedral crystals, mostly forming aggregates with apatite and monazite, that border metasomatized biotite; metasomatic zircon crystals occur at the border of spongy-textured metasomatic titanite (Fig. 3e, f, h, i); (5) apatite crystals vary in size from small euhedral crystals (50 µm), usually forming aggregate with other accessories, up to 300–500 µm (possibly metasomatic); these minerals are occasionally included in fresh biotite while commonly form aggregate in close contact with deeply metasomatized biotite (chlorite–titanite–rutile–phlogopite; Figs. 3e, 4h); (6) iron sulfides, chalcopyrite, and minor Zn–Pb sulfides occur as fracture and cavity infill (Fig. 1 in ESM).

Endoskarn Endoskarn bodies are a system of tabular (Fig. 2d), disoriented (Fig. 1c) bodies crosscutting the main pluton and connected to the exoskarn aureole. The endoskarn bodies include a few remnants of the original granite (i.e., plagioclase, quartz, and minor K-feldspar) and an abundance of metasomatic minerals (phlogopite, chlorite,

titanite, diopside, calcite, minor epidote, rutile, apatite, and zircon). Biotite is completely replaced by a diopside–phlogopite–titanite–chlorite association, as well as by accessory minerals. These formed as multiple generations and include HFSE–REE minerals (up to 5 vol %; epidote), Th–U-bearing minerals, sulfides (up to 5 vol %; pyrrhotite replaced by pyrite, chalcopyrite, arsenopyrite, and sphalerite), and adularia infilling fractures, evidence for K mobilization. The abundance of diopside decreases from core to rim coupled with the increasing abundance of titanite (local Ti circulation vs. efficient circulation of Fe and Mg). Occasionally, centimetric euhedral crystals of titanite occur in veins along with diopside and quartz. These crystals show a range of textures, from homogeneous to patchy zoned, together with multiple cracking and sets of fluid inclusions (Fig. 4). The epidote group is represented by two terms: a greenish, Fe-rich, and patchy zoned epidote with dissolution/recrystallization textures, usually replaced by brownish to black, REE-rich allanite (Fig. 4e). The crystallization of calc-silicates is followed by the generation of a calcite–chlorite–fluorite–sulfides assemblage. Fluorite is widespread in veins and inclusions, occasionally replacing biotite along cleavages (Figs. 3f, 4b). Phyllic alteration (chlorite–sericite) is generally significant in the endoskarn core, where the abundance of iron sulfides and fluorite is higher, and calc-silicates are commonly replaced by late zircon, thorite, and uraninite.

Exoskarn Pervasive metasomatism in the marble host clearly overprints the earlier contact metamorphic structures (Fig. 2a, e–g; Vezzoni et al. 2016). Irregular massive bodies occur at the pluton–marble contact, with patches of marble relics inside the exoskarn, while other bodies result from selective replacement of ductilely folded marly layers within the marble (Fig. 2a, e, f). Exoskarn masses are locally observed connecting with endoskarn aligned bodies (Fig. 2a). The metasomatic minerals are mainly represented by diopside, garnet, vesuvianite, titanite, phlogopite, minor scapolite, adularia, and allanite. Accessory minerals include zircon, apatite, magnetite, pyrrhotite replaced by pyrite, minor chalcopyrite, sphalerite, and arsenopyrite, together with multiple generations of fluorite. Some minerals, such as quartz and calcite, are found in almost all skarns, with calcite abundance decreasing toward the pluton. On the other hand, variable abundances of metasomatic minerals allow to distinguish different types of contact endoskarn, moving from the granite to the marble: (a) proximal diopside–titanite–phlogopite rocks; (b) vesuvianite > garnet rocks; (c) garnet > vesuvianite rocks; (d) phlogopite–titanite–albite–diopside rocks replacing folded marble; (e) wollastonite-rich rocks, replacing vesuvianite-garnet rocks, at the exoskarn-marble contact. Diopside and red vesuvianite show massive to radiating textures, amazingly regular zoning, as well as secondary metasomatic textures close to the pluton/marble contact (i.e., vesuvianite and early REE-rich

epidote replaced by late REE-poor epidote). Garnet dominantly occurs as either granoblastic aggregates or less common euhedral crystals, red-to-brown in color, with concentric growth zones, with no consistent compositional trends. Titanite is widespread in the exoskarn bodies (slight increase close to the granite contact), commonly with patchy zoning and spongy textures. Phlogopite abundance increases significantly in specific layers, thus indicating that the original limestone layering may have been one of the governing factors in its origin. Exoskarn bodies mimicking marble folded levels show the highest abundance of metasomatic phlogopite (> 50 vol %). Epidote group minerals (including allanite) are widespread in all these bodies as both prograde and retrograde mineral. Abundances of accessory HFSE–REE and Th–U minerals increase close to the granite boundaries, where accessory calc-silicate such as epidote, allanite, ekanite ($ThCa_2Si_8O_{20}$), as well as apatite are formed. These minerals are frequently replaced by apatite, zircon, thorite, uraninite, as well as quartz and fluorite. Moreover, secondary accessories resulted from the alteration of early calc-silicates, such as titanite. Indeed, such minerals are frequently bordered by uraninite, thorite, and zircon (Fig. 4i). High-to-low-temperature sulfides (i.e., pyrite, pyrrhotite, chalcopyrite, and sphalerite) are widespread throughout the exoskarn system (Fig. 1 in ESM).

Late hydrothermal veins A low-temperature hydrothermal vein system crosscut the granite body (Fulignati 2018). This late manifestation is characterized by abundance of chlorite, low-temperature sulfides, calcite, quartz, and fluorite, as well as accessory HFSE–REE and Th–U-bearing minerals (Fig. 1 in ESM). Late-crystallized anhydrous minerals such as quartz are observed as minor interstitial minerals. The main sulfides are pyrrhotite, pyrite, sphalerite, chalcopyrite, and minor galena. Single- and poly-phase sulfide grains are observed filling open-spaces, forming veins, or as isolated crystals, and showing multiple intergrowth and mutual replacement textures Individual grains are typically subhedral and varying from μm to cm in size.

Borehole samples (petrographic variation with depth)

The analysis of several exploratory borehole logs (Samim 1983), reaching the main pluton at different depths, has been performed to investigate the lithological variations with depth through the carbonate host to the granite. We then focused on the MS3 borehole, cored from the metamorphosed carbonate rock through a thick metasomatized body to the granite, which has been reached at 225 m below the surface (Fig. 2 in ESM).

Pure marble extends from the surface to about 170 m depth. This is a medium to coarse-grained white–pink marble, with common grey impurities due to increasing marly component and decreasing grain size. The marble
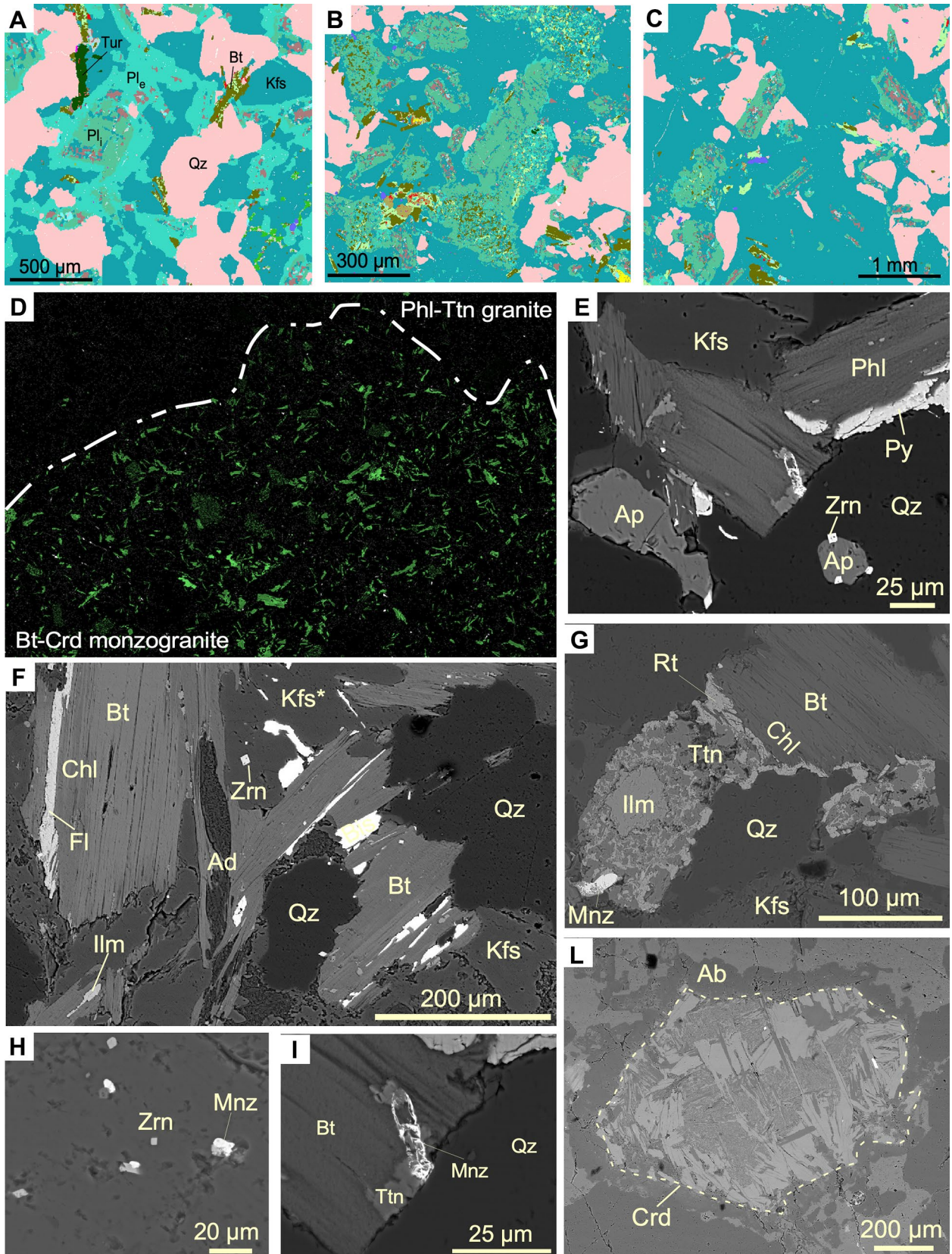
◄**Fig. 3** QEMSCAN and backscattered electron image showing metasomatic processes in the granite. **a–c** QEMSCAN images showing the alteration of plagioclase from cordierite–biotite granite (**a**) to increasingly metasomatized granite (**b**, **c**). Secondary K-feldspar replace plagioclase (Plg$_i$ = An$_{35-45}$, Plg$_e$ = An$_{10-15}$). Biotite is replaced by Chl–Ttn–Phl, while ilmenite is replaced by Ttn–Rt aggregates. **d** QEMSCAN Fe distribution element map at contact between metasomatized and cordierite–biotite granite. **e–g** Backscattered electron images of biotite infilled by fluorite and late sulfides, showing replacement by chlorite, phlogopite, and titanite. In **g**, ilmenite is replaced by titanite and rutile. Apatite and zircons occur both in biotite and its border. **h**, **i**, **l** Backscattered electron images of metasomatic and replacement accessory minerals. **h** Metasomatic monazite and zircon in secondary K-feldspar. **i** Relict of monazite in biotite (magnification of **e**. **l** Pinitized cordierite in monzogranite. For abbreviations, see Whitney and Evans (2010)

presents some disequilibrium geometries such as granoblastic sutured textures, with dominant calcite, dolomite (increasing with depth), minor quartz, phyllosilicates, and sulfides. Between 50 and 120 m, widespread metasomatic phlogopites occur, accompanied by minor K-feldspar, rare diopside, accessory fluorite, chlorite, and muscovite (exoskarn).

Between 170 and 220 m, several metasomatic minerals are observed, mostly represented by calc-silicate aggregates, whose abundance increases towards the pluton contact. From top to bottom, aggregates of phlogopite, K-feldspar, scapolite, and plagioclase are replaced by fine-grained exoskarn bodies, predominantly characterized by diopside, phlogopite, K-feldspar, minor vesuvianite, garnet, and scapolite. Secondary minerals are epidote, fluorite, chlorite, and sulfides. A minor mineralization with pyrite and magnetite is also present. Closer to the granite contact the modal amount of garnet and epidote increases, while diopside is frequently found together with scapolite and vesuvianite.

At ca. 225 m, the drill core enter the pluton, made of three rock subtypes: (1) a brownish-pinkish leucogranite (superficial granite) mainly characterized by K-feldspar (50 vol %), quartz (30 vol %), plagioclase (10–15 vol %), and phlogopite-titanite assemblages (5–10 vol %); this section is characterized by millimetric-to-centimetric veins, mainly consisting of quartz, chlorite, fluorite, calcite, and sulfides; (2) between 320 and 400 m (mixed zone), a petrographic and chemical variation has been observed linked to the occurrence of a series of aligned endoskarn bodies, mainly characterized by diopside, titanite, phlogopite, and epidote, accompanied by late sulfides, calcite, and chlorite; (3) between 400 and 550 m (deep granite) the borehole goes through a slightly metasomatized granite (variable replacement of biotite by titanite–chlorite–phlogopite), with the final 70 m mainly made by biotite-rich granite.

Results: geochemistry of the main lithologic types

Whole-rock analyses from the main representative lithologies (cordierite–biotite granite, metasomatized granite, endoskarn, exoskarn, and marble) allow to better characterize the process of element mobility occurred at the pluton–marble contact during metasomatic processes. Moreover, the comparison with borehole data (Samim 1983) allows to identify geochemical variations with depth and to relate them to petrographic data. Samples, originally collected from drill cores at 3 m intervals, did not directly bracket metasomatic alteration boundaries or lithological contacts. Compositional data for major elements have been obtained on whole rock by XRF at the Rimin laboratory during exploratory investigations (Samin 1983), while trace elements have been determined by ICP-MS on acid-digested powders.

Botro ai Marmi mine

Whole-rock compositions of the outcropping lithologies are reported in Supplementary Tables. The granite has a syenogranitic-to-monzogranitic composition (SiO$_2$ = 70–72 wt%) and a peraluminous character (ASI = 1.1–1.3). The CIPW normative assemblages, as well as other major and trace element features, show clear similarities to other peraluminous igneous products from southern Tuscany (i.e., Gavorrano, Montecristo Island, and Giglio Island intrusions; Dini et al. 2002; Pinarelli et al. 1989; Poli and Peccerillo 2016).

The comparison between the original granite and the metasomatized granite has been performed using decreasing SiO$_2$ as an index of progressive alteration. Indeed, silica content significantly decreases from the cordierite–biotite granite (71–69 wt%), to the metasomatized granite (66–64 wt%), and to the endoskarn bodies (55 wt%). Ca and P exhibit a significant correlation with silica; indeed, silica decrease is accompanied by increase in endoskarn and in the metasomatized granite (Fig. 5a). This process corresponds to titanite and diopside crystallization during potassic–calcic metasomatism. A quite similar pattern is defined by K variations, which shows the same values for cordierite–biotite granite and endoskarn. The silica versus potassium diagram shows a characteristic composition for the granite, with K$_2$O values between 5 and 8 vol % possibly related to plagioclase/K-feldspar volume by volume substitution. Values of potassium higher than 8 vol % have been related to pervasive crystallization of adularia as vein infill and metasomatic masses (Fig. 5b). Mg, Ti, and Al values are almost constant throughout. Silica increase corresponds to MgO/FeO$_t$ ratio increase, linked to the almost complete replacement of biotite by phlogopite (Fig. 5c). Na$_2$O does not show significant correlation
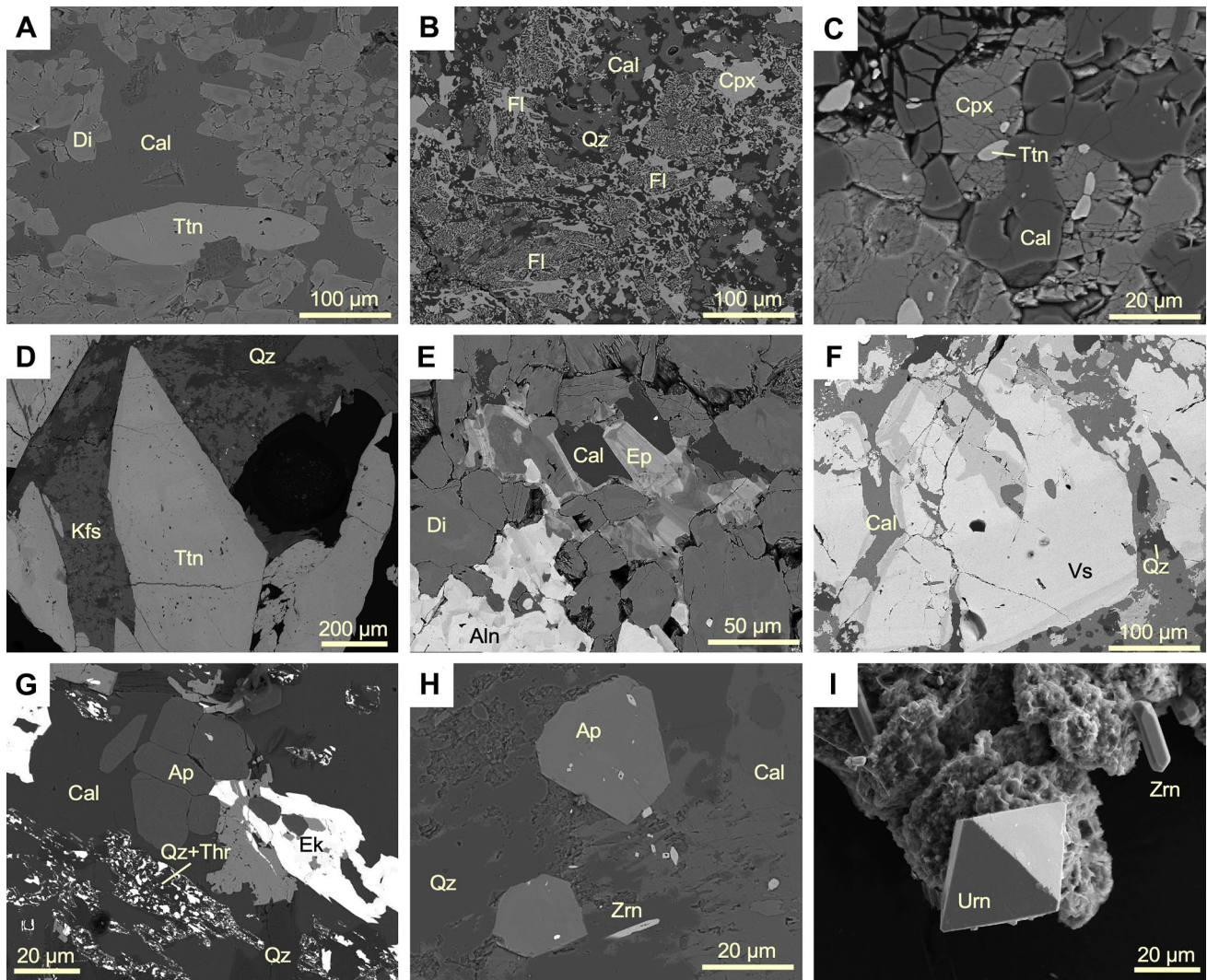
Fig. 4 a Filling fractures diopside–titanite and late calcite exoskarn. **b** Fluorite–calcite–quartz–diopside pseudomorphs in Cpx-rich exoskarn. **c** Dissolution texture of diopside and titanite, with late calcite. **d** Euhedral zoned titanite with relict K-feldspar and quartz, in endoskarn. **e** Late allanite replacing epidote in Di-rich exoskarn. **f** Zoned vesuvianite with fractures filled by REE-enriched overgrowth. **g** Pseudomorph of thorite–quartz after ekanite, with apatite, quartz, and calcite in Cpx-rich exoskarn. **h–i** Apatite, zircon, and uraninite resulting from metasomatic alteration of biotite (**h**) and titanite (**i**) in endoskarn

versus silica (Fig. 5d), while Sr, Rb, and Ba variations show a negative linear correlation versus silica.

The transition from the original granite to the metasomatized granite is characterized by the decrease of FeO_{tot} from values of about 2.5 wt% to values lower than 0.25 wt%. FeO_{tot} increases significantly in the endoskarn bodies (up to 10 wt%). Higher values of FeO_{tot} are coupled with an increase of Al_2O_3 content up to 21 wt% (15–16 wt% in the original granite). The same systematic variation is also observed for MgO. The abundance of TiO_2 is constant in both the metasomatized and cordierite–biotite granite (0.35–0.45 wt%). Na content decreases with the alteration, while K increases from the original granite to the phlogopite–titanite granite (from 5 up to 10 wt%). Na/K ratio shows

a positive correlation with Sr and negative correlation with Rb values. The endoskarn bodies, in which plagioclase is completely replaced by K-feldspar, show the maximum value of K. The abundances of Rb and Ba show a positive correlation with K_2O, and in some samples of the metasomatized granite Rb and Ba rise over 500 ppm. The CaO value increases from 1 to 2 wt% in the original granite to 3 wt% in the metasomatized granite. A net increase occurred in the endoskarn bodies, up to value of 10 wt%. Th concentration increases from 14 ppm in the cordierite–biotite granite to 18 ppm in the metasomatized granite (up to picks of 24 ppm), while decreases in the endoskarn to 9 ppm. Initial U concentration decrease from 12–14 to 4 ppm, with metasomatic alteration.
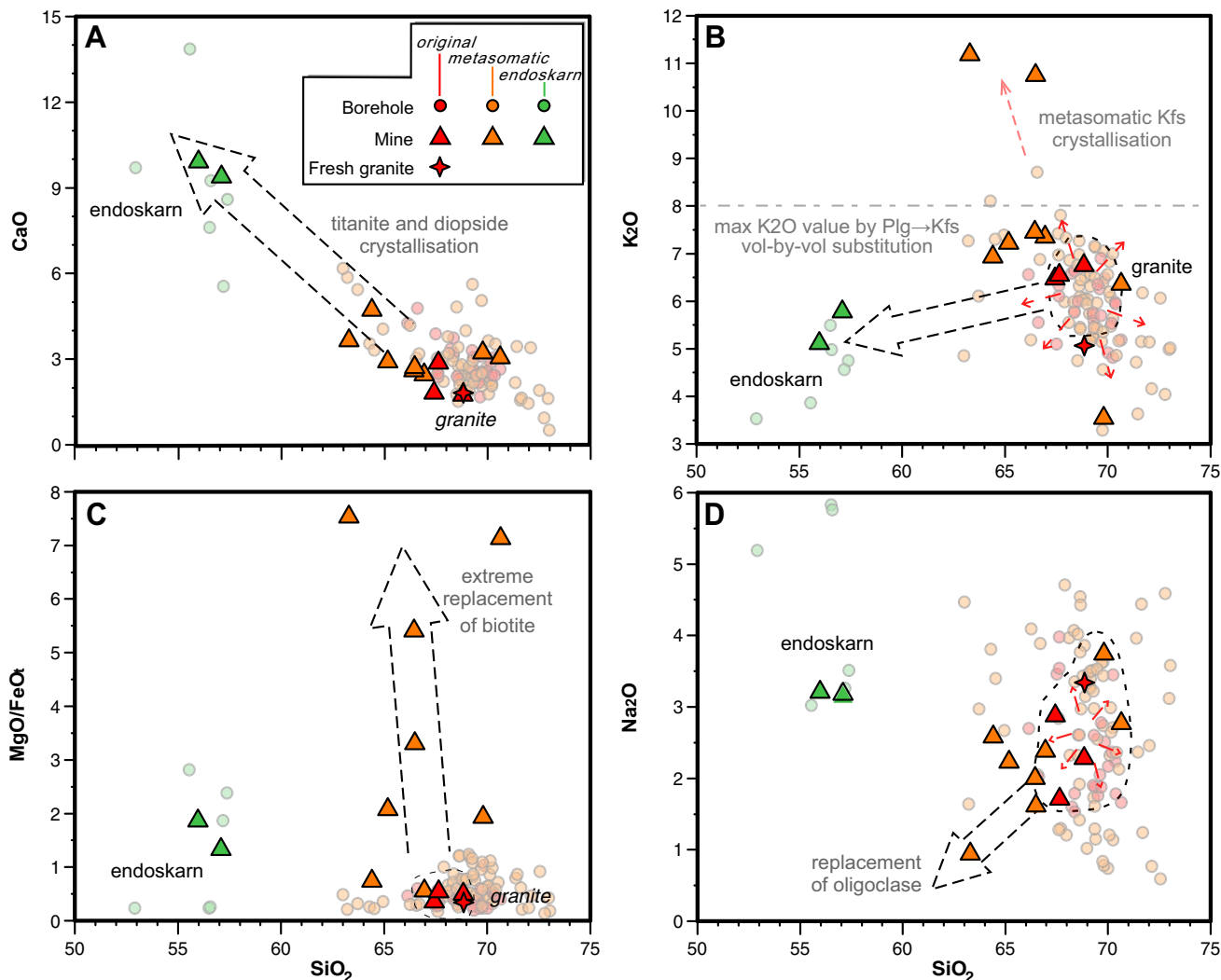
Fig. 5 Selected oxide diagrams for the Botro ai Marmi cordierite–biotite granite (red), metasomatized granite (orange), and endoskarn bodies (green). Triangles indicate samples collected at the Botro ai Marmi mine (this study); the white circle indicates samples from the *MS3* borehole (Samim 1983); the red star indicates the monzogranite initial composition (*sample GBM5*). The grey arrows highlight the effects of the alteration processes characterized by loss of silica and iron accompanied by gain of K_2O and CaO

The exoskarn bodies show an increasing silica content moving to the pluton–marble contact, from 40 up to 50 wt%. Total Fe and Mg show maximum values of 20 and 13 wt%, respectively, in the vesuvianite–garnet-rich exoskarn. Ti shows common values of 0.25–0.3 wt%, with maximum amount of 0.8 wt% in the phlogopite-rich exoskarn. K_2O and Na_2O show low values in all the exoskarn bodies (lower than 1 wt%). The CaO content, values from 20 to 24 wt%, shows a positive correlation with distance from the pluton, except for the phlogopite-rich exoskarn, showing common values of 7–9 wt%. Th and U are lower than 3 ppm.

The Botro ai Marmi granite exhibits fractionated pattern of rare-earth elements (REE) and moderate Eu anomaly (Eu/Eu* = 0.55–0.60), similar to those reported for other peraluminous bodies from southern Tuscany (Fig. 6a; Dini et al. 2002, 2005; Poli and Peccerillo 2016; Ridolfi et al. 2016). The pattern of the endoskarn sample has slightly more fractionated (light) LREE, with Eu anomaly (Eu/Eu* = 5.3 respect to ~ 20). Patterns for the phlogopite and vesuvianite–garnet-rich exoskarn show even more significant LREE fractionation along with minor (heavy) HREE fractionation. Marble shows a comparable pattern, although at significantly lower concentration. The phlogopite-rich exoskarn presents a strong positive anomaly of Y, while the pyroxene-rich exoskarn shows significant LREE fractionation and upward-concave HREE pattern, and strong negative anomaly of Y (Fig. 6a). Thus, Y appears decoupled from lanthanides in phlogopite-rich and pyroxene-rich exoskarn, in opposite ways.
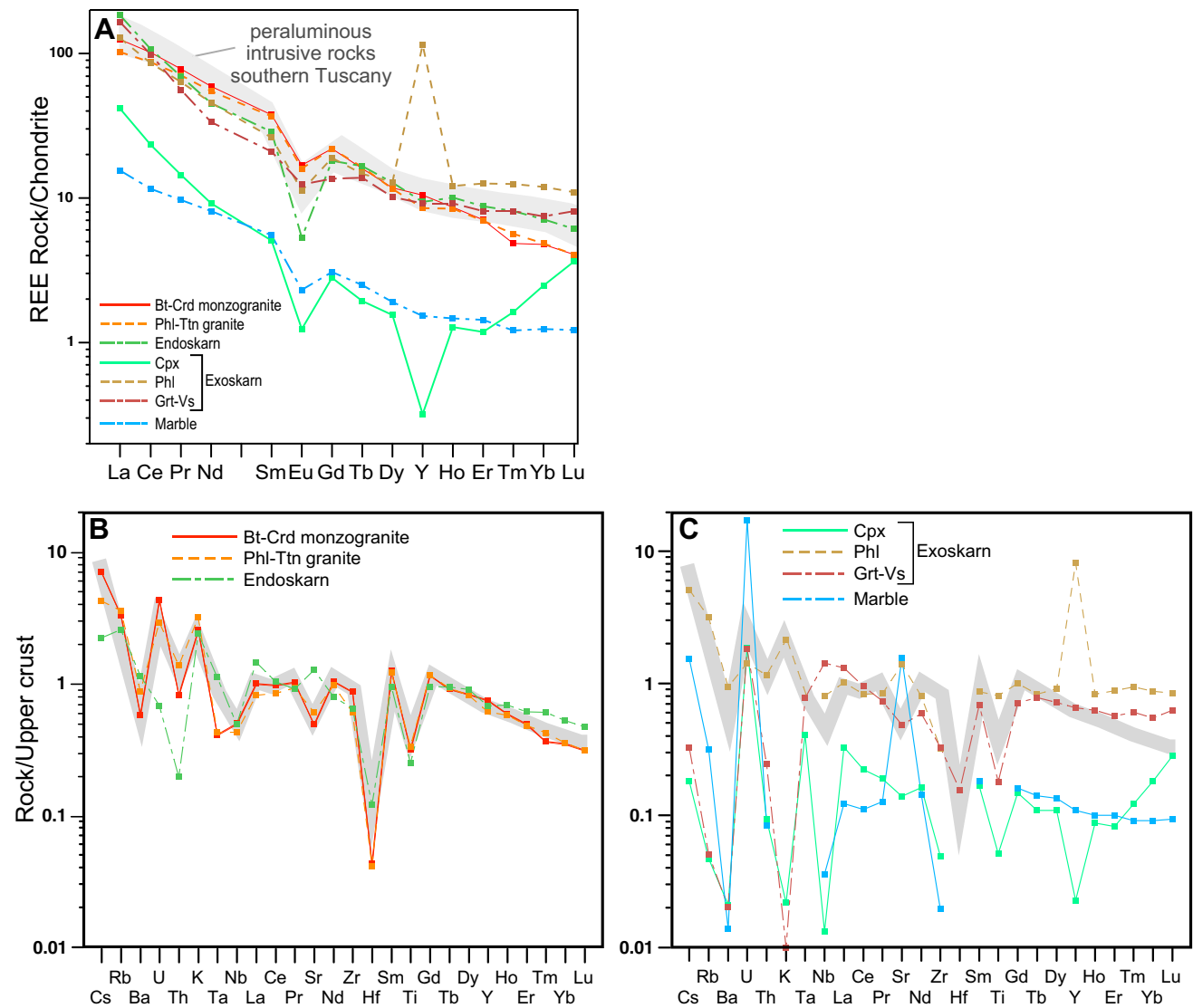
Fig. 6 **a** Chondrite normalized REE patterns for Botro ai Marmi granite, endoskarn, exoskarn, and marble. The shaded field represents the REE composition of the peraluminous intrusive rocks from southern Tuscany (after Pinarelli et al. 1989; Poli and Peccerillo 2016). Normalising values after Sun and McDonough (1989). Upper crust normalized multi-element spider diagrams. **b** Granitic rocks from

Botro ai Marmi compared with the composition of the peraluminous intrusive rocks from southern Tuscany (shaded field; after Poli et al. 1989, Poli and Peccerillo 2016). **c** Comparison between the lithologies observed at the Botro ai Marmi mine. Normalising values after Sun and McDonough (1989)

The continental crust-normalized multielemental patterns for the granite (Fig. 6b) show, again, characteristics common to crustal products from southern Tuscany (Dini et al. 2002, 2005; Poli and Peccerillo 2016; Ridolfi et al. 2016). These include positive anomalies for U, K, and Rb, together with negative anomalies for Ba, Hf, Sr, and Ti, as well. Endoskarn bodies show comparable patterns, except for a marked negative Th anomaly. The exoskarn bodies show strongly variable elemental distributions (Fig. 6c). The phlogopite exoskarn has a pattern mostly

similar to the granite. The garnet–vesuvianite exoskarn has elemental distribution quite similar to the granite, with the notable exception of very low contents for Cs, Rb, Ba, and K. The pyroxene exoskarn has a peculiar elemental distribution, quite similar to the marble for progressively less incompatible elements, including very low Nb, while the extremely low abundances of Cs, Rb, Ba, and K are similar to those of garnet–vesuvianite exoskarn. Thorium is progressively depleted from granite, through endoskarn, to garnet–vesuvianite then clinopyroxene exoskarn.

Borehole samples (geochemical variations with depth)

The relative concentrations of elements vary with depth, underlining the occurrence of boundaries of metasomatic alteration fronts and/or lithological contacts (Figs. 7, 8). The pure marble shows a net decrease of the CaO/MgO ratio with depth, which corresponds to an increase in dolomite/calcite ratio, moving from massive limestone to stratified black limestone, and it is accompanied by the overall decrease in Sr from high concentration (up to 900 ppm) in the marble (Fig. 8). Zinc shows maximum concentration at the top of the core (up to 500 ppm) and decreases with depth, and it is linked to the occurrence of small Zn-bearing minerals, such as hemimorphite-$Zn_4Si_2O_7(OH)2H_2O$ and sphalerite-ZnS
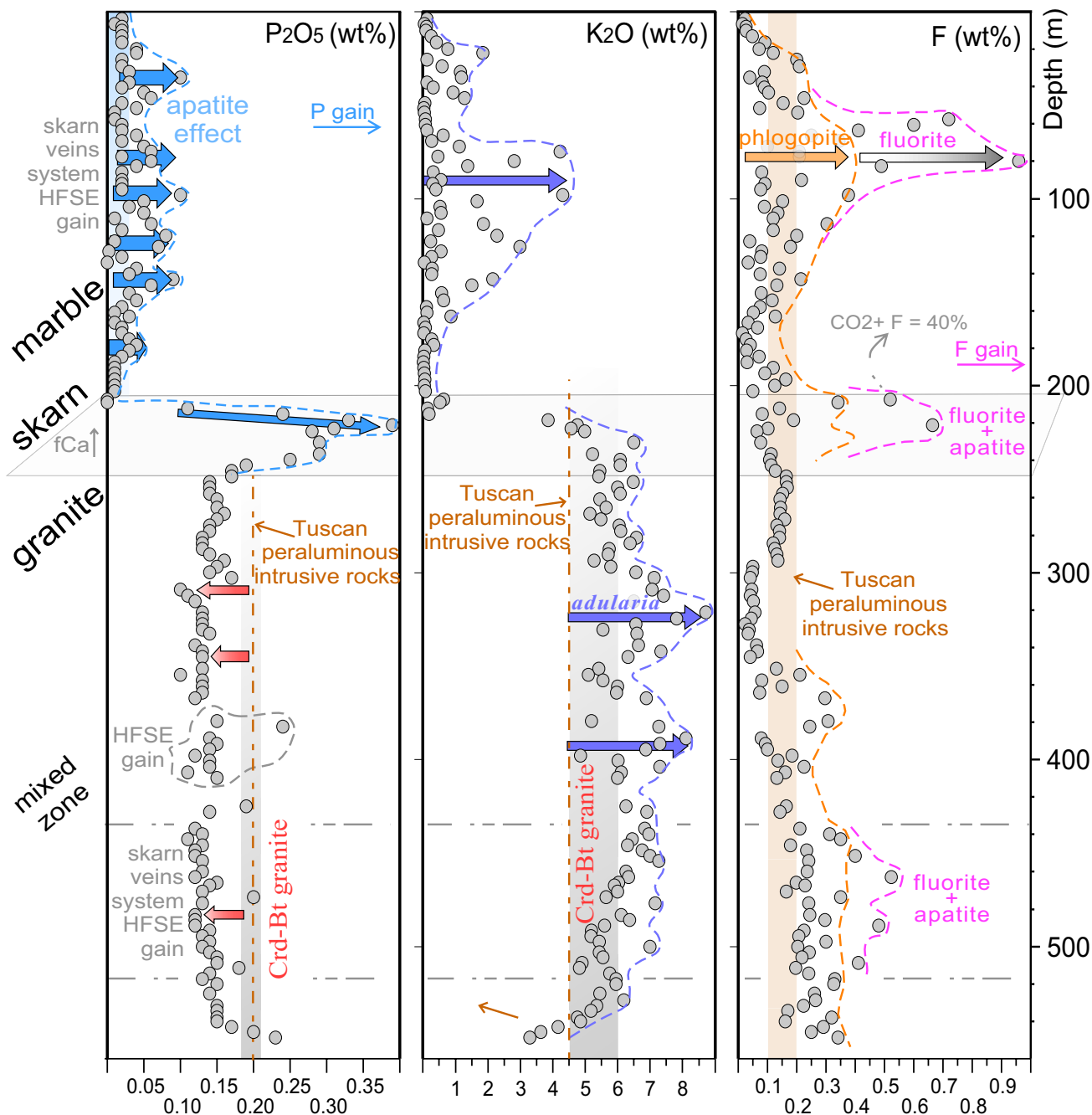

Fig. 7 P_2O_5, K_2O, and F (wt%) variation with depth in the MS3 borehole. The dashed lines indicated the mean composition of the cordierite–biotite granite (red) and of the peraluminous intrusive rocks from southern Tuscany (black). The arrows indicate the progressive crys-tallization of apatite (blue), adularia (violet), phlogopite (yellowish), and fluorite (magenta). Values of Tuscan peraluminous intrusive rocks are from Poli and Peccerillo (2016)
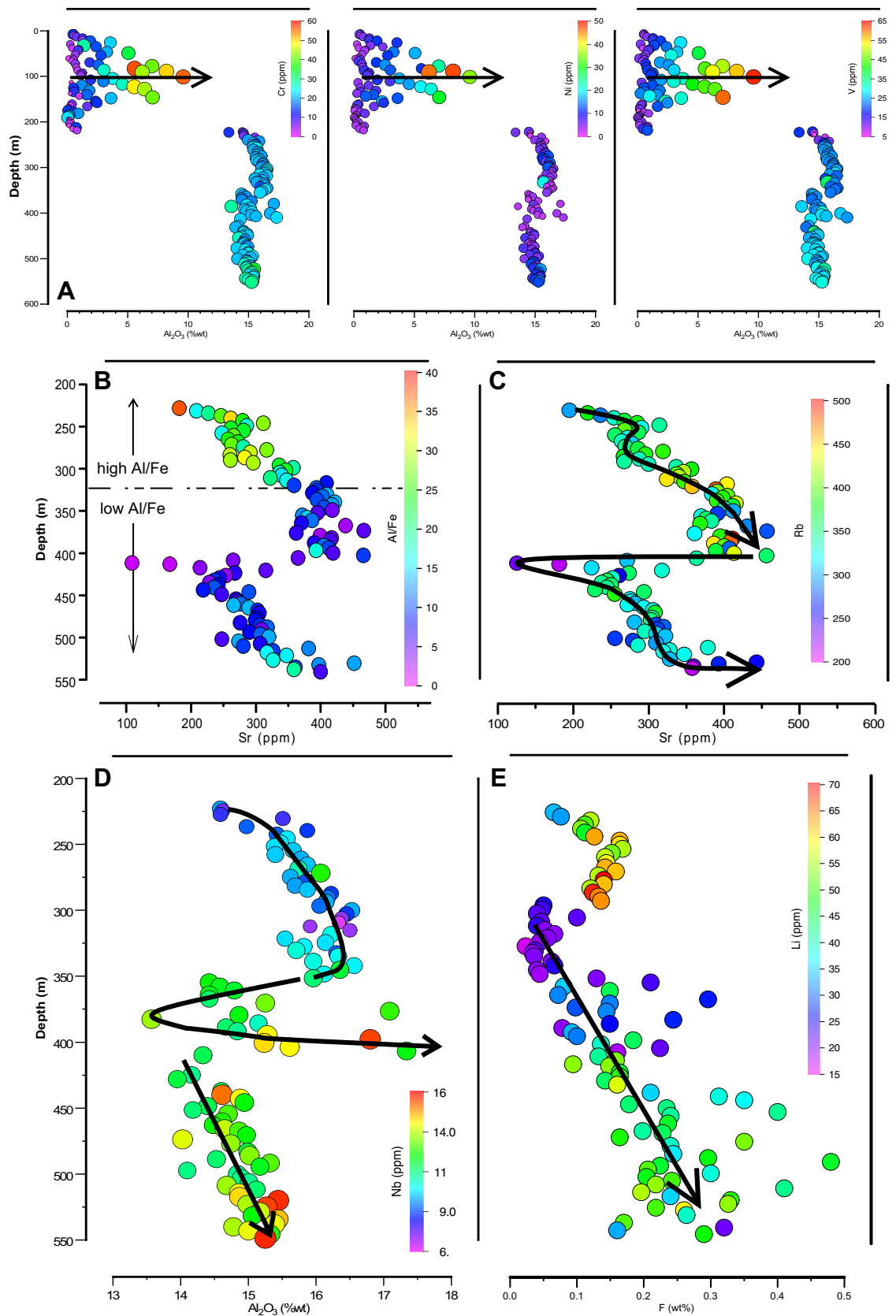
Fig. 8 Selected diagrams showing the geochemical variation with depth in the MS3 borehole. Major elements oxides as wt%, trace elements as ppm. Arrows indicate the main patterns

(Samim 1983). Li and F values show a positive correlation, increasing in correspondence of pyrrhotite and scheelite mineralization.

The transition between exoskarn and Crd–Bt granite is marked by few meters of endoskarn, and the high values of Fe, Cu (up to 800 ppm), and F (up to 5 wt%), correspond to mineralization of pyrrhotite, fluorite, and minor chalcopyrite (Samim 1983). Tin reaches values up to 700 ppm in correspondence of endoskarn bodies crosscutting the granite and containing cassiterite, adularia, green fluorite, pyrite, and garnet. Scattered increases of Zn, Pb, Cu, and S correlate with pyrite–sphalerite–galena mineralization (Samim 1983). In detail, between 180 and 220 m, a fine-grained exoskarn occur (Samim 1983), with high values of Fe and Cu, corresponding to pyrrhotite–pyrite–magnetite mineralization. Between 80 and 150 m, the scattered concentration peaks of Co, Cr, Ni, Nb, Rb, V, Ti, Y, Zr, and Zn correspond to mineralized exoskarn bodies (Figs. 7, 8).

In the granite body, Sr shows a significant positive correlation with depth (Fig. 8b, c). The superficial granite from the Botro ai Marmi mine shows values of about 200 ppm, increasing with depth up to 500 ppm in the mixed zone (400 m), where it drops to 100 ppm (Fig. 7). The deepest granite is characterized by a trend similar to the superficial granite, with values of 100–200 ppm at 420 m, increasing up to values of 400–450 ppm at 550 m. Nb values follow the same trend (Fig. 8d). Aluminum, like Sr, shows a clear increase with depth in the upper part of the granite, from 15.0 to 16.5 wt%, variable values in the mixed zone (from 15.5 to 17.5 wt%), and the same trend as Sr in the deep granite. The Al_2O_3/FeO_{tot} ratio shows high values in the superficial granite (until ~ 300 m), then decreases in the mixed zone, coupled with Fe-rich calc-silicate crystallization (Fig. 8b).

Analyzing the overall profile, it is possible to observe (Figs. 7, 8): (1) the abrupt increase of K_2O in the marble (~ 100 m), corresponding to metasomatic phlogopite-rich layers, (2) the high values of K_2O for the bulk of the granite (5–9 wt%), except for the cordierite–biotite granite at the surface and at depth in the borehole (3.5–4.0 wt%), corresponding to a widespread replacement of plagioclase by K-feldspar and adularia; (3) the general increase of F concentration with depth, and prominent peaks corresponding to both exoskarn and endoskarn, that are characterized by fluorite and phlogopite crystallization (phlogopite effect); actually, the crystallization of phlogopite account for F values lower than 0.3–0.4 wt%, and thus, it is required the crystallization of fluorite to reach higher values; (4) P_2O_5 peaks of 0.1 wt% in the marble (against overall content of 0.02 wt%), and 0.35 wt% in the granite (against overall content of 0.15–0.2 wt%), correlate with exo-/endoskarn where apatite is observed to crystallize (apatite effect); high values of P_2O_5 and F correspond to HFSE increase, that is also related to crystallization of vesuvianite, garnet, allanite, titanite, apatite, and ekanite.

Discussion

Mineralogical evolution from magmatic to metasomatic stages

The evolution of the Botro ai Marmi magmatic–metasomatic–hydrothermal system can be subdivided into multiple stages based on different rock textures and mineral assemblages: a magmatic stage, a potassic–calcic metasomatic stage, and a final acidic metasomatic stage (Fig. 9). In this context, relatively simple mineralogical patterns are overprinted by multiple metasomatic events. Reactive transport models are generally too poorly constrained to offer unique solutions, while equilibrium calculations are at best an approximation. Even in systems where local fluid–rock equilibrium is not attained; however, reactions generally progress along a vector similar to that defined by equilibrium models. Equilibrium models can, therefore, provide a qualitative indication of system behavior (Meinert et al. 2005). Here, a genetic interpretation is proposed for the mineral assemblages observed at Botro ai Marmi, explaining the relations between different mineral paragenesis and different metasomatic stages. Here, a typical high-temperature metasomatic activity (temperatures between 500 and 550 °C; Franzini et al. 2010; Fulignati 2018) developed at the contact with the pluton. As supported by literature data, the metasomatic paragenetic sequence observed at Botro ai Marmi indicates crystallization temperatures between 550 and 350 °C.

Magmatic stage The timing of magmatic feldspar crystallization is critical for the understanding of any following process. Compositions and textural observations indicate the presence of at least two generations of igneous plagioclase. The first generation is represented by normally zoned crystals (An_{35-45}), later slightly resorbed and overgrown by an oligoclase rim (An_{10-15}), interpreted as a second-generation feldspar according to the neat compositional gap against the andesine cores (Fig. 3a–c). This zoning jump requires a physical change in melt conditions, affecting the stability of andesine to the point where oligoclase would nucleate. A sudden decrease in pressure is a viable driving mechanism (e.g., Plümper and Putnis 2009) to generate these two-stage textures. During the first stage, plagioclase (An_{35-45}) crystallized early in the magmatic body together with biotite, K-feldspar, quartz, cordierite, as well as accessory zircon, apatite, and ilmenite. In the second stage, rapid ascent with sudden pressure drop allowed the crystallization of a thick oligoclase rim over andesine plagioclase. Late exsolution of B-rich fluids resulted in the crystallization of tourmaline–quartz orbicules. This event is terminated by the local
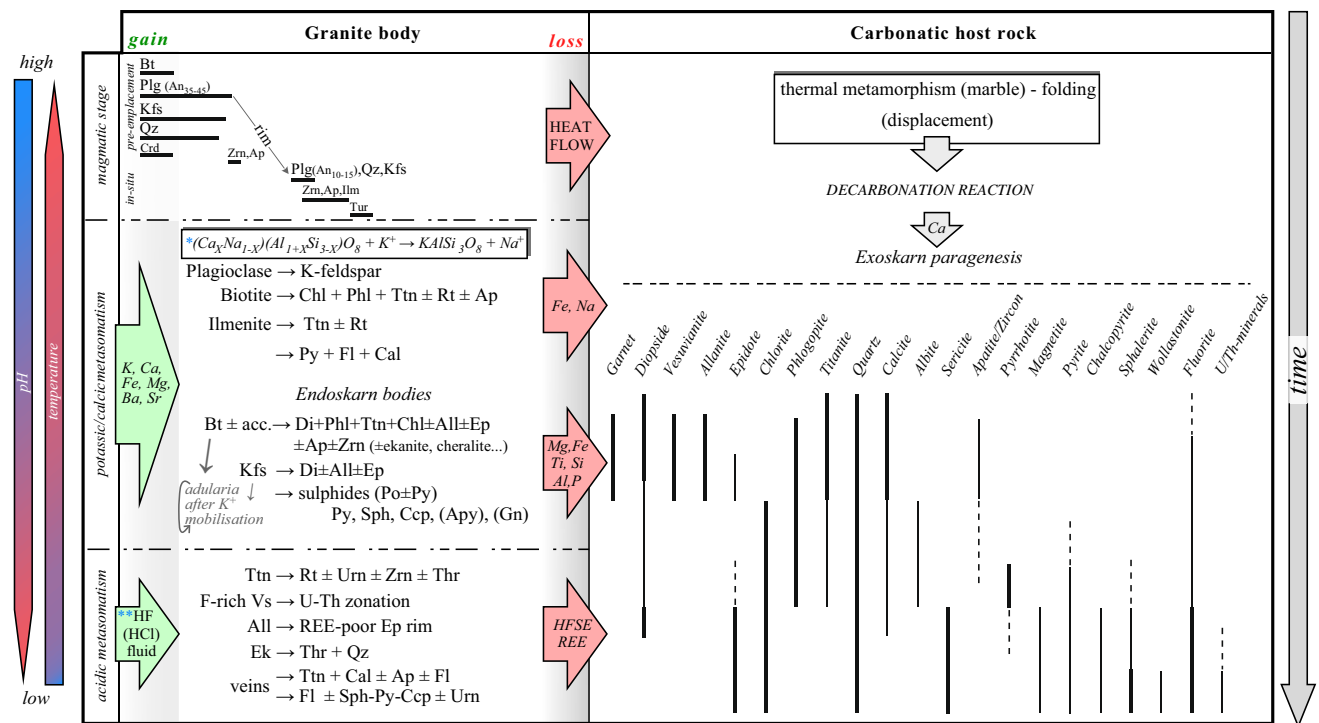
Fig. 9 Mineral paragenesis summarising the original and metasomatic mineralogy from the granite body and the carbonate host rock. *Plg rim (An$_{10-15}$) completely replaced by Kfs, while Plg core (An$_{35-45}$) partially replaced. **calc-silicates dissolution/replacement, HFSE and REE local mobilization, chemical zoning (i.e., Vs, Ttn, Di, and Grt)

circulation of residual B-rich fluids along fractures with formation of hydrothermal tourmaline–quartz veins (they are cut by later skarns). Like the other TMP granite pluton, the emplacement/crystallization of Botro ai Marmi pluton triggered the formation of the contact aureole transforming the limestone host into a marble (Vezzoni et al. 2018).

Potassic-calcic metasomatism After emplacement and crystallization, the cordierite–biotite granite was affected by an intense, pervasive potassic–calcic metasomatism (Fig. 4). Chemical potential gradient (or chemical activity) in the rock-pore system control the distribution of fluids/elements and, thus, of the metasomatic products, into the granite body and at the pluton/host contact. There, the redistribution of elements in both directions results in the replacement of both the rocks.

Potassic metasomatism Affected the whole granite body, leading to the almost complete replacement of cordierite–biotite granite (K-feldspar, andesine-An$_{35-45}$, oligoclase-An$_{10-15}$, quartz, biotite, and minor ilmenite–apatite–zircon–monazite) by phlogopite–titanite granite (K-feldspar, andesine-An$_{35-45}$, phlogopite, chlorite, titanite, and minor rutile–apatite–zircon–monazite–fluorite). Calcic metasomatism affected the monzogranite mostly along magmatic joints, and at the contact with the host marble (Fig. 2a, d). The preferential circulation of fluids along magmatic joints led to the development of endoskarn aligned bodies,

characterized by significant replacement of the original magmatic paragenesis by Ca(–Mg)-silicates including diopside, phlogopite, chlorite, and titanite, along with minor epidote and calcite.

The most noteworthy reactions resulted from the circulation of alkali-rich fluids. Indeed, in a closed system subject to thermal gradients, K/Na activity ratio of a fluid in equilibrium with two alkali feldspars at high temperature would be higher than that of a fluid in equilibrium with the same assemblage at lower temperature. If such a system was open, infiltration of fluid from a higher temperature environment to a lower temperature environment would promote replacement of sodium in the granite by potassium from the fluid. Thus, complete replacement of oligoclase, and partial replacement of andesine by K-feldspar could be ascribed to a mechanism of alkali ion exchange between fluid and feldspar phases controlled by a replacement reaction (e.g., Orville 1963; Moore and Liou 1979):

$$\left(NaAlSi_3O_8\right)_{solid} + \left(K^+\right)_{aq} \rightarrow \left(KAlSi_3O_8\right)_{solid} + \left(Na^+\right)_{aq}.$$
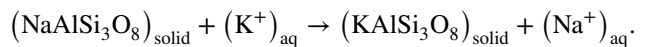
Irregularly shaped K-feldspar, which has a composition similar to the K-feldspar in the original granite, is found mostly as replacing the oligoclase rim, suggesting that oligoclase was converted directly to K-feldspar. Plagioclase abundance decreases from about 30 vol % in the original

granite to 5 vol % in the metasomatized granite. The reaction between oligoclase and fluid implies the mobility of Al^{3+} (that may be incorporated in sericite), Na^+, and Ca^{2+}. The elements released by the reaction might have been accommodated in calcite, epidote, and fluorite. Isotropic replacement of oligoclase by K-feldspar supports a pervasive circulation of fluids between grain boundaries. The same evidence is highlighted by crystallization of metasomatic minerals along the igneous grain boundaries. Moreover, loss of sodium from oligoclase could explain the observed local crystallization of albite. The degree of metasomatic alteration increases with distance from the cordierite–biotite granite relics, while the local gain in Si corresponds to crystallization of albite and quartz.

During this stage, biotite is completely replaced by aggregates of phlogopite (50%), chlorite (30%), and titanite (20%), which has been later partially converted to rutile (Fig. 3g); in endoskarn bodies, where calcium activity is prominent, the replacement of biotite and feldspar resulted also in the crystallization of diopside and other calc-silicates (Fig. 4). Parry and Downey (1982) describe the hydrothermal alteration of biotite considering both iso-volumetric and Al-conservative reactions. They conclude that the process proceeds at constant Al and requires variable additions of K and Mg, as well as significant subtractions of Fe. Thus, the alteration would result in a significant volume loss (up to 30%), which is, however, compensated by the products of concurrent reactions (titanite, rutile, minor quartz, and adularia). Mg^{2+} ions were added, while Fe^{2+} ions were lost. The overall reaction keeps constant $Ti + Al$ within the pseudomorphic chlorite–titanite–phlogopite assemblage. Fe^{2+} likely contributes to the crystallization of new Mg–Fe calc-silicates in the contact exoskarn bodies. Moreover, the accessory minerals included in biotite are affected by intense metasomatic alteration.

On the other side, the metasomatic replacement along endoskarn bodies is most prominent, showing higher concentration of calc-silicates correlated with the highest Ca and Mg contents. These reactions promoted mass transfer of Si and Mg. On the contrary, deeply metasomatized granite at the contact with endoskarn shows the highest values of K and the complete replacement of plagioclase by K-feldspar and sericite. At the same time, the increase of Rb, Ba, and Sr values, with Na decrease, is linked with K-feldspar crystallization. Thus, simultaneous reactions involving oligoclase, K-feldspar, biotite, and accessory minerals converted the original paragenesis to a new Ca-rich mineral association. Starting from the mineral assemblage of the original monzogranite, a significant input of Mg and Ca is required to produce the resulting endoskarn bodies.

At pluton-marble contact, the metasomatic replacement advanced in both directions resulting in the pervasive overprinting of bedded marble by a banded exoskarn and in the replacement of the granite by a massive endoskarn body. The presence of carbonate alteration zones provides evidence that metasomatic fluids in these systems could generate their own skarn mineral assemblages. However, the abundance of Fe–Mg-rich calc-silicates and enrichment in K, Ba, Sr, Rb, in the metasomatized samples, support the contribution of fluids from an external source. Indeed, the marble, composed essentially by calcite, dolomite, and minor white mica, has been replaced by assemblages of diopside, grossular garnet, vesuvianite, allanite, titanite, phlogopite, and minor scapolite. The distribution of these minerals reflects the relative mobility of major elements and, to a lesser extent, the host carbonate composition. As an example, the occurrence of Mg-rich phlogopite exoskarn, along previously folded marble levels, may be related to a highest abundance of marly impurities (mica-rich fraction). These observations highlight the selective process of circulation of Fe and Mg penetrating several meters into the marble. On the contrary, Ti, usually an immobile element, shows a local prominent mobilization. Indeed, abundant crystallization of titanite and rutile occurred in close spatial relation with deeply metasomatized biotite (Fig. 4). In the endoskarn bodies, titanite is more abundant at the border, decreasing towards the core. On the contrary, titanite abundance decreases in distal exoskarn (Phl-rich exoskarn). Sulfides, occurring as fracture infill, in disrupted primary cavities and brecciated portions of the metasomatic bodies, post-date the formation of the calc-silicate skarns.

Thus, the Botro ai Marmi system underwent input of Ca, Si and mostly of Mg and Fe from an external source. This implies a relative decrease in concentration for immobile elements. This element input is concurrent with the formation of calc-silicates and the release of CO_2 by the decarbonation reaction (Harlov and Austrheim 2013). The interaction between monzogranite and CO_2-rich fluids, released during calc-silicate reactions, can explain the high K and Ba, and to a lesser extent, Sr abundance in the metasomatized granite. Assimilation of marble country rocks can account for the high Ca and Sr contents observed in the metasomatized samples. However, this process can only justify Ca and Sr abundances in granite samples very close to the granite/wall–rock interface. In fact, the assimilation is limited by the amount of heat available and by the surface area of the assimilated rocks (Durand et al. 2009). These observations, coupled with the Mg and Fe-rich nature of metasomatic minerals, point to an origin of hydrothermal fluids at least partly from an external mafic igneous source as also inferred for the adjoining Temperino mining area (Vezzoni et al. 2016).

Acidic metasomatism The increasing acidity of circulating fluids, possibly related to mixing with acidic fluids released at depth by the granite body, is testified by patchy zoning (i.e., titanite), as well as dissolution–recrystallization textures, pseudomorphs, and pronounced zoning in

calc-silicates (Figs. 2, 3, 4). Acidic metasomatism could be responsible for the intense alteration of accessory minerals included in biotite (apatite, zircon, monazite, and ilmenite), as testified by aggregates of euhedral accessory minerals (apatite, zircon, and monazite) bordering deeply metasomatized biotite crystals. Moreover, strongly chloritized biotite commonly hosts fluorite crystals in interlayer positions. The crystallization during this stage of Ca-REE-rich minerals, such as allanite, ekanite, and cheralite, lends support to the mobilization of HFSE/REE by fluids characterized by increasing acidity (Fig. 4). Moreover, the continuous crystallization of calc-silicates (Ca sequestration) increases the acidity of the fluids, leading to the alteration of earlier calc-silicates with diffuse crystallization of accessory minerals (e.g., thorite, uraninite, and zircon), usually on their surfaces or in fractures (Fig. 4i). Again, F-rich fluid circulation is supported, in endoskarn, by pseudomorph textures developed as fluorite–pyroxene–calcite–quartz aggregates replacing diopside–calcite–quartz assemblages (Fig. 4b), or in exoskarn, by the pseudomorphic replacement of Ca-REE-silicates (Fig. 4g; ekanite replaced by thorite–quartz pseudomorphs). The abundance of quartz-fluorite veins associated with crystallization of HFSE–REE and Th–U accessory mineral aggregates (veins and inclusions) indicates that this stage postdated potassic–calcic metasomatism. The acidic metasomatism extended into the surrounding host rock and involved the formation of minerals filling fractures in the granite, in the endoskarn at the pluton–marble contact, and in the exoskarn bodies. The ubiquitous presence of fluorite in skarn, granite, and quartz–fluorite veins suggests that acidic, F-rich fluids circulated in the system during the whole metasomatic activity. Finally, data from quartz-hosted fluid inclusions from the Botro ai Marmi granite, containing high NaCl and KCl contents (Caiozzi et al. 1998; Fulignati et al. 2018), show that Cl fluids should be taken into account for the increasing acidity of the system and for the progressive mobilization of REE (Gysi and Williams-Jones 2013; Gysi et al. 2016).

Accessory minerals (REE and HFSE mobility) As commonly observed in peraluminous granites, the content of REE and HFSE is linked to the abundance of accessory minerals, which are mostly included in biotite or other phyllosilicates (Clarke 1981; Villaseca et al. 2012). Peraluminous granites from Tuscany are no exception, with most accessory minerals included in biotite (e.g., Dini et al. 2005). Thus, the metasomatism of phyllosilicates could promote the mobilization of HFSE and REE into the system. At Botro ai Marmi, this process of HFSE–REE mobilization is mostly attributed to acidic, F(–Cl)-rich fluids for a sum of evidence: (1) the common occurrence of fluorite interlayered in the biotite structure, generating a focused chloritic alteration; (2) the process of dissolution/precipitation of accessory minerals, that commonly recrystallized at or across the rim of biotite; (3) the abundance of unusually large apatite, as well as small euhedral monazite and zircon bordering metasomatized biotite; (4) monazite is uncommon in biotite, except for a few crystals showing pseudomorphic textures, while it is commonly found as 5–20 μm crystals in interstitial K-feldspar and quartz, or forming trails of crystals in interstitial K-feldspar (10–15 μm monazite–zircon aggregates); (5) zircon is the accessory mineral most resistant to metasomatic alteration processes, according to its abundance in both fresh and metasomatized biotite, with the most significant evidence being the crystal shape and size: zircons included in biotite are usually rather large (50 up to 200 μm) and show variable euhedral shapes, whereas those found at the border of biotite or in endoskarn are usually smaller than 30–50 μm, showing morphological features such as lack of prismatic faces, absent or rare inclusions, pointing out that these small zircons are the product of late, low-temperature crystallization (Schaltegger 2007).

Recent works show that a neat hydrothermal origin for apatite and zircon can be inferred by their occurrence in exoskarn bodies. Extensive evidence has been obtained for hydrothermal zircon crystallized from volatile-rich partial melts metasomatized mantle, beneath old continental roots, later sampled incidentally by kimberlite (Griffin et al. 2000). Finally, little evidence exists for hydrothermal zircons derived from metasomatism of a granitic rock (Yang et al. 2009; Park et al. 2016) and no evidence for hydrothermal zircons from metasomatic alteration of a peraluminous granite body is reported. In this context, recognizing the hydrothermal nature of zircon could be pivotal in reconstructing metasomatic processes by U–Pb dating. U–Pb dating of reliably identified hydrothermal zircon would complement less precise and multiply biased U–Pb ages of apatite, monazite, rutile, and titanite from hydrothermal–metasomatic deposits (Fig. 10).

Elemental gain/loss during metasomatism

When igneous rocks are modified to a large extent by metasomatic processes (addition/removal of several elements), the chemical composition and mineralogy underwent progressive changes. Thus, any overall model must accommodate information from studies addressing different aspects of fluid evolution. In this study, we have developed mass-balance calculations for the amounts of elements added and/or removed. During alteration, the volumes of plagioclase and biotite decrease, and phlogopite replaces biotite, while K-feldspar replaces oligoclase, increasing in abundance. Such calculations also have to consider the density and volume changes, because the newly formed minerals in the granitic rocks have different densities and volumes from those in the original rock. Some assumptions also have to be made, i.e., whether to balance the chemistry assuming that at least
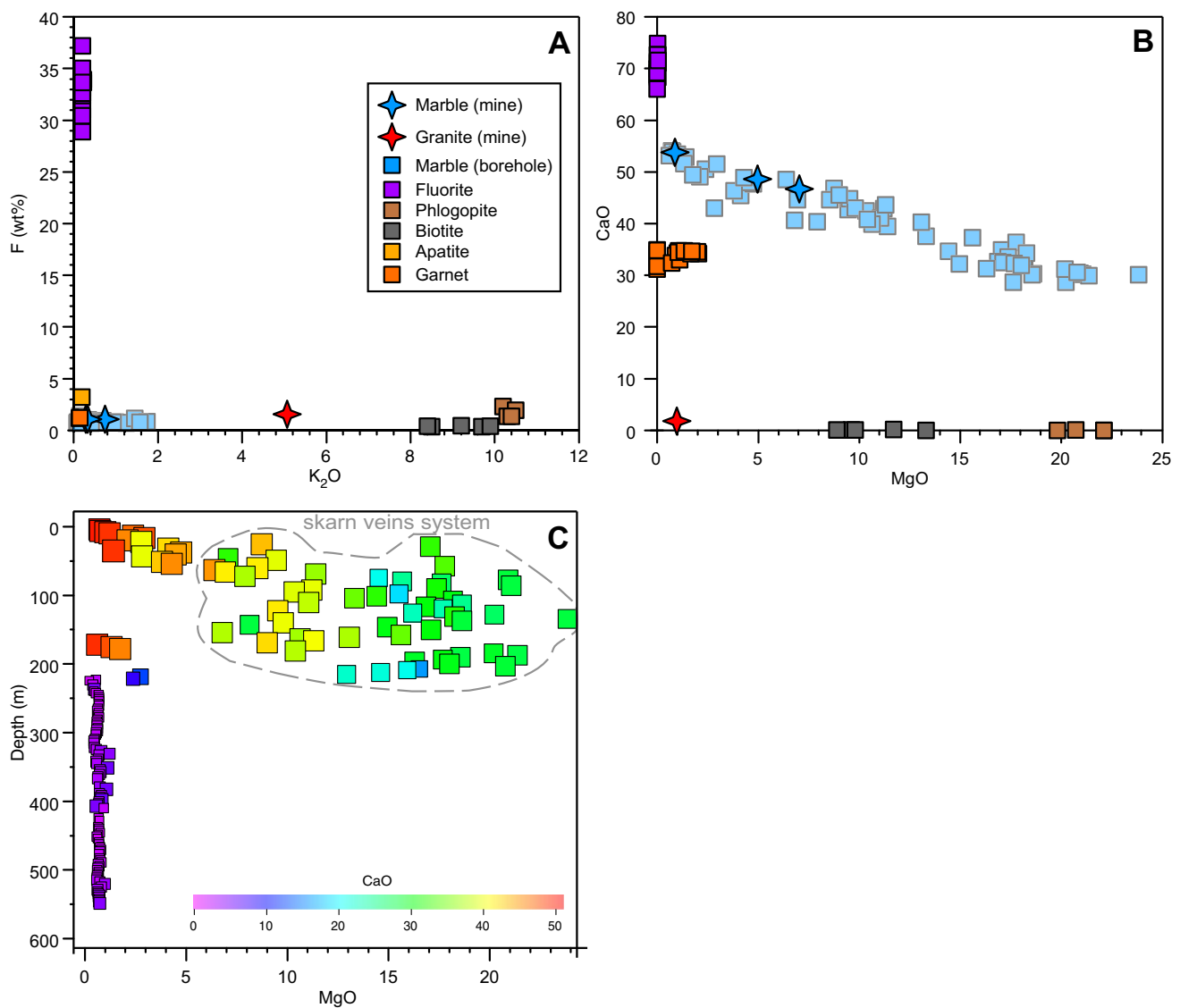
Fig. 10 **a**, **b** Comparison between compositions of marble (both from borehole and mine), granite, biotite, and the main representative metasomatic minerals (fluorite, apatite, phlogopite, and garnet). **c** MgO vs. CaO distribution in the MS3 borehole

one element is immobile (e.g., Baumgartner and Olsen 1995; Grant 1986, 2005; Gresens 1967; López-Moro 2012). Geochemical observations and isocon diagrams (Baumgartner and Olsen 1995; Grant 1986, 2005) help to quantify the relative loss, gain, or immobility of elements during the alteration processes, by comparing the chemical composition of fresh (original) and metasomatized samples. The original composition of the granite has been selected according to petrographic and geochemical observations (Fig. 5). The representative pristine sample has been collected as far as possible from the contact against the metasomatized granite and looks unaffected by metasomatism as indicated by the occurrence of fresh biotite crystals. The pristine composition has been compared with the metasomatized granite (phlogopite–titanite granite), exoskarn and endoskarn (Fig. 11a,

b) using isocon diagrams. The selection of immobile elements for isocon diagrams construction is performed according to cluster of slopes or volume factors, as suggested by López-Moro (2012). In each diagram, a best-fit isocon, an isocon at constant mass, and an isocon at constant volume are reported.

Original granite vs. metasomatized granite The comparison between c*ordierite–biotite granite* and *phlogopite–titanite granite* results in very limited volume and mass changes (<1%). Total Mg and Ti do not show significant variations (Fig. 11a). An explanation for Ti invariance could be its redistribution from biotite in the cordierite–biotite granite, to titanite in the metasomatized granite. This interpretation is supported by the gain of Ca, which is, in turn, supported by gain of P (apatite crystallization). The massive loss of Fe,
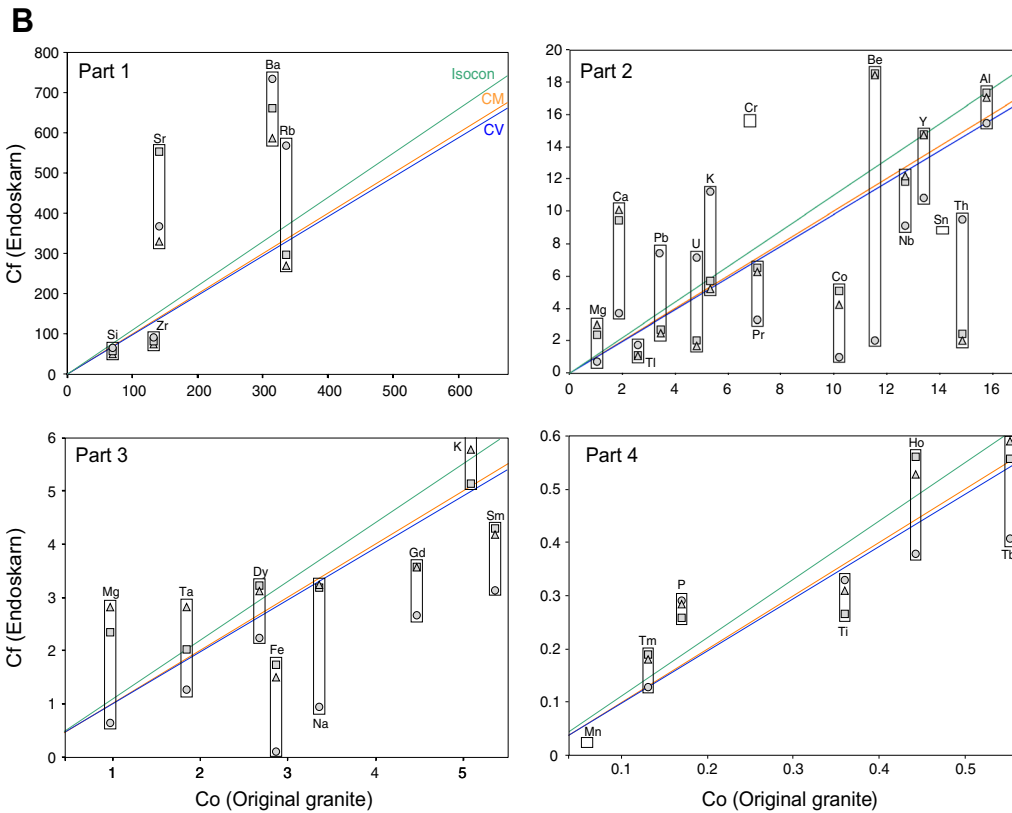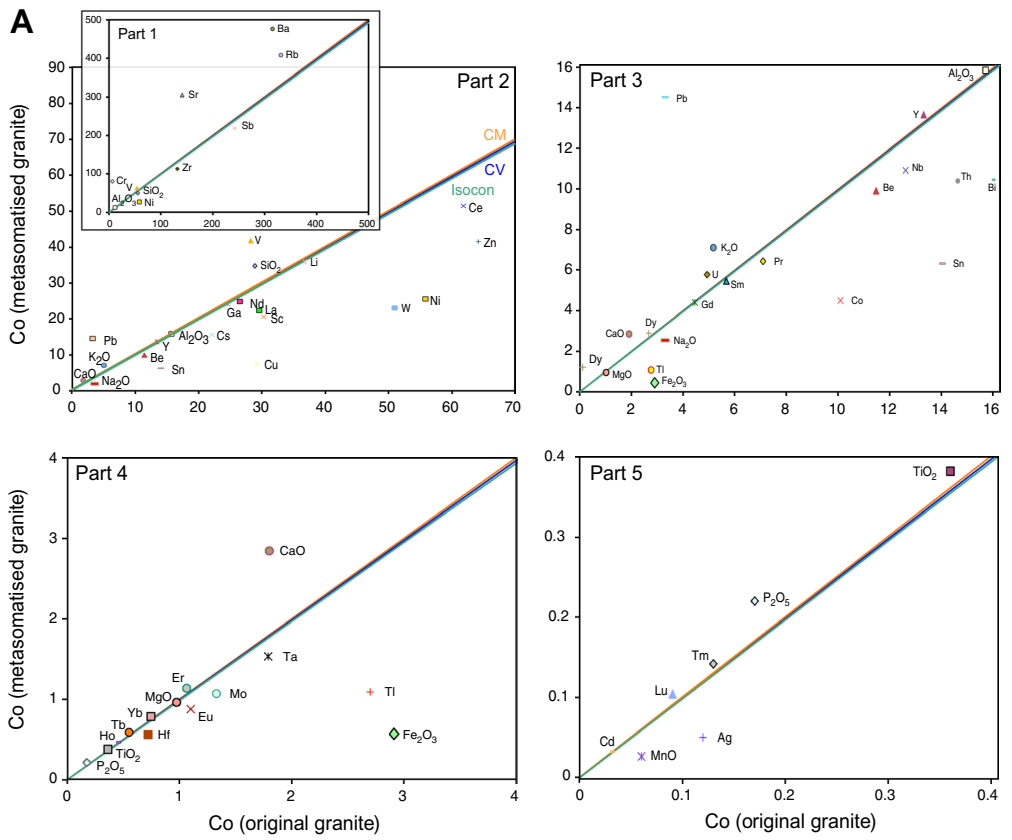
◄**Fig. 11** Main isocon diagrams of cordierite–biotite granite against: **a** phlogopite–titanite granite (Ti as immobile element) and **b** endoskarn bodies (Si as immobile element) from rim (circle) to middle (square) and to core (triangle). In both the diagrams, the quantification of volume changes and mass-balance modeling has been realized according to López-Moro (2012). The selection of immobile elements for isocon diagram construction is performed according to clusters of slopes and/or volume factors (López-Moro 2012). Green: best-fit isocon; blue: isocon at constant mass; orange: isocon at constant volume

the significant loss of Na, and the gain of K are driven by the complete alteration of biotite and the oligoclase replacement by K-feldspar in the metasomatized granite. The significant crystallization of K-feldspar could also explain the Rb and Ba enrichment. Indeed, Rb is rather compatible in K-feldspar and biotite, but highly incompatible in plagioclase. Moreover, the positive correlation between Sr and Na/K and the negative correlation between Rb and Na/K ratio are compatible with plagioclase replacement by K-feldspar. Moreover, because the composition of metasomatized rocks is likely to be somewhat variable as a consequence of accessory mineral abundances, the concentrations of trace elements give valuable insights. The main evidences are the general loss of metals (Cu, Zn, Zr, Ni, Mo, Sb, and Tl) and the major depletion of Sn and W in the metasomatized granite (Fig. 11a). On the other hand, the results obtained from samples from the borehole evidenced the loss of Mg, Cr, Ni, Nb, and Sr with increasing depth (Figs. 7, 8, 10), probably linked to the increasing metasomatic alteration of biotite and K-feldspar (replaced by adularia).

Original granite vs. endoskarn The element mobility resulting by the replacement with endoskarn is prominent (Fig. 11b). The resulting overall mass and volume losses are about 5%. Si and Na show a significant loss, mostly resulting from the replacement of plagioclase by K-feldspar. Biotite leaching caused a massive Fe loss. The apparent Ca, Al, Mg, P, and K gain is likely to be caused by both the acidic and potassic metasomatic processes. In detail, diopside and apatite crystallization is likely responsible for Ca, Mg, and P gain, while metasomatic K-feldspar is the better candidate to account for the gain of Al and K. As observed for the phlogopite–titanite granite, Rb, Ba, and Sr are gained during the metasomatic processes, while metals are lost. Endoskarn, from borders to core, shows increasing loss of Si, K, Rb, Ba, and Sr probably resulting from the replacement of K-feldspar by albite. On the contrary, the gain of Fe, Mg, Ca, and Na is likely linked to the massive crystallization of calc-silicates at the core of endoskarn bodies. Moreover, spike of REE could be ascribed to the crystallization of accessory allanite. The other trace elements remain almost unvaried (Fig. 12).

Marble vs. exoskarns Chemical mass transfer has been quantified between the original composition of the marble and the exoskarn products. The marble protolith composition has been calculated by averaging three analyses of pristine marble samples from the host rock. The samples have been collected as far as possible from the contact against the monzogranite and appear unaffected by metasomatic processes. On the other hand, exoskarn bodies are mainly characterized by metasomatic diopside, vesuvianite, titanite, phlogopite, garnet, epidote, quartz, and accessory apatite, zircon, and fluorite. Geochemical data suggest an overall strong decrease of Ca and Sr (up to 70%), correlating with the decrease of calcite content as the pluton contact is approaching. A significant gain of Si, Fe, Mn, Ti, as well as Cr, Sc, and Zn is linked to calc-silicate crystallization. The gain of REE, Y, and Zr can be ascribed to the crystallization of HFSE/REE accessory minerals (e.g., zircon and allanite) and of REE-rich calc-silicates (e.g., vesuvianite and titanite). The contents of W, Sn, Pb, and other metals increase toward the contact with the intrusion, showing the lowest values in the garnet–vesuvianite skarn. The Al content increases from diopside, through garnet–vesuvianite to phlogopite-skarn, correlating with phlogopite abundance. P content is strictly related to the abundance of apatite, which increases in phlogopite and garnet–vesuvianite skarn. The REE distribution, as observed in endoskarn, is mostly related to calc-silicates and accessory minerals abundance. For example, the enrichment in La and Ce is petrographically testified by allanite crystallization. Usually, diopside exoskarn shows a loss of REE (except for La, Ce), while phlogopite and garnet–vesuvianite skarns show REE gain, with positive anomalies of HREE. Garnet, with its high partition coefficients for HREE (Gaspar et al., 2008), is a good candidate to account for the gain of HREE. Thus, garnet contains most of the HREE budget of the whole rock. Moreover, as supported by field and petrographic observations, the phlogopite-rich exoskarn preferentially replaces folded marble (marly layers). Comparing marble and exoskarn, it emerges that (1) the gain of Rb, Sr, Ba, K, and Al correlates with phlogopite, K-feldspar, and albite new crystallization, (2) the prominent depletion in Ca corresponds to the consumption of calcite, with Ca that is partially leached away from magmatic-hydrothermal solutions (see Kwak and Tan, 1981), (3) a strong gain of metals and trace elements such as Sn, W, Sb, and Nb did occur, and (4) the significant gain of LREE correlates with the crystallization of accessory allanite, which has a very high partition coefficient for LREE (Bea 1996; Herman 2002). The mineralogical and geochemical evolution from marble to exoskarn documents the elemental transfer during metasomatism. The general volume loss, up to 25% for the Grt-Vs skarn, probably resulting from marble decarbonation, never correlates with significant mass loss. Indeed, the increase of the density (up to 70% in the Grt-Vs skarn), due to new calc-silicate crystallization, compensates the mass loss resulting from the decarbonation process.
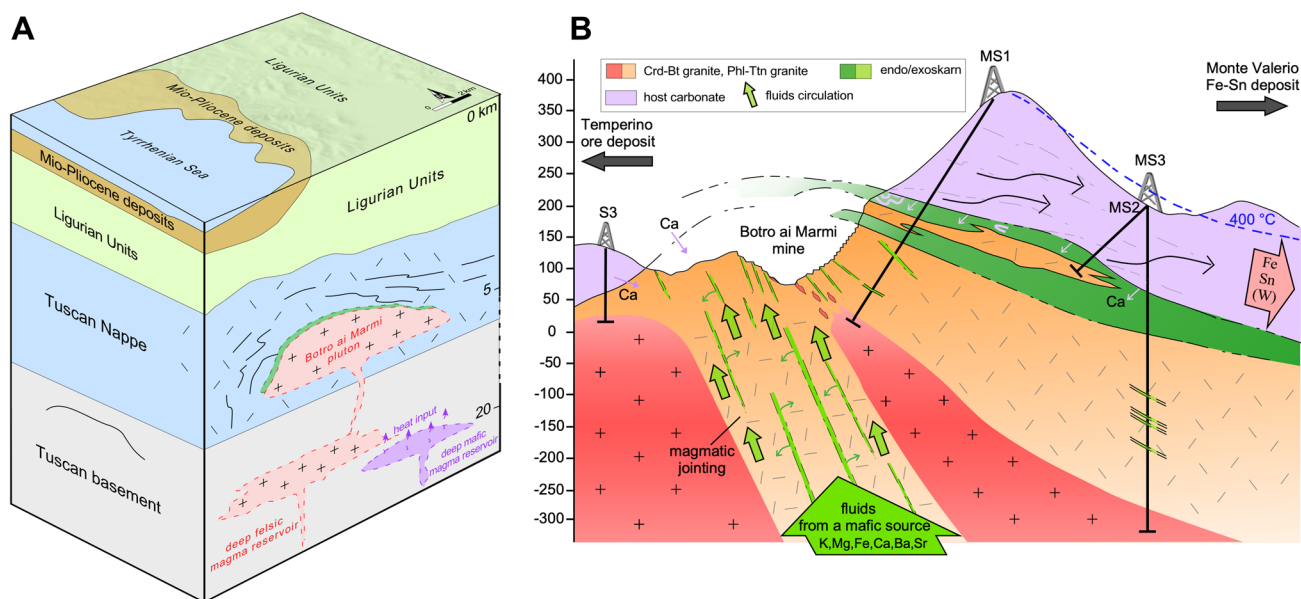
Fig. 12 Schematic cartoon for the metasomatic alteration of the Botro ai Marmi peraluminous monzogranite and carbonatic host. The magmatic jointing promotes the circulation of K-rich fluid (black) and Ca-rich fluid (green) in the granite body, while the foliation and folding allow the formation of the contact exoskarn in the host

Summary and comparison of elemental circulation during metasomatism

The comparison of the isocon diagrams allows to speculate on the origin of the metasomatic fluids. Gain of Mg, Ca, K, and, to a lesser extent, of Sr, Ba, and Cr in the metasomatized granite and in the endoskarn supports a possible release of fluids from a mafic magma. Loss of Fe, Co, Th, and strong circulation of Ti and REE in the granite result from the metasomatism of biotite and accessory minerals which it includes. Overall, the metasomatized granite shows enrichment of those elements that are leached from the endoskarn and depletion of some elements that are rather in endoskarn body, which, moreover, is enriched in elements that necessarily came from an external source.

Complex metamorphic–metasomatic–hydrothermal effects in multi-pulse intrusions

The high-temperature reactions activated during and following the granite intrusion in the country rock are quite a complex sequence, characterized by the superposition of various mineralization patterns resulting from multiple metasomatic events. A sequence of mineral assemblages and a change in bulk chemical composition can be traced from the un-metasomatized marble towards the granite body, and it can be related to specific metasomatic processes. Petrographic and geochemical data show that the question about the nature and source of metasomatic fluids is not easily answered.

Among possible hypotheses that can be formulated, multiple sources are likely the best option.

First of all, such data are typical of potassic metasomatism commonly affecting porphyry (Seedorff et al. 2005) and epithermal mineralizing systems (e.g. Serifos Island, Ducoux et al. 2017). These systems are characterized by replacement of plagioclase by orthoclase, breakdown of biotite, and growth of new micas (phlogopite) and adularia (e.g., Pirajno 2009), as well as sulfide formation (chalcopyrite, pyrite, and molybdenite). The process of potassic metasomatism in porphyry-type mineralization is thought to be triggered by fluids extracted from magmas of intermediate compositions (mostly latitic-to-andesitic) and calc-alkaline to high-K calc-alkaline affinity (Sillitoe 2010). On the other side, peraluminous plutons worldwide are mostly associated with Sn skarns. The least Al-saturated plutons have the thermal and chemical activities to form Ca–Fe skarns, which usually show a significant mantle signature and relatively little interaction with continental sedimentary material (Meinert et al. 2005). Pyroxene and garnet–pyroxene skarns typically resulted from interaction between metasomatic fluids released by a mafic–ultramafic source and a carbonatic host rock (e.g., Meinert et al. 2005). Skarn replacing more or less pure marble tends to be more Ca-rich, with minerals such as hedenbergite, ilvaite, and johansennite as observed at the Temperino mine (Vezzoni et al. 2016).

At Botro ai Marmi, a peraluminous monzogranite intruded an almost pure marble host. The crystallization of new metasomatic minerals corresponds to a general gain of K, Ca, Fe, and Mg. The main metasomatic minerals are

K-feldspar, phlogopite, titanite, diopside, vesuvianite, and grossular (typical of mafic metasomatism). Fluids released from an external source as to be invoked to explain the high K, Fe, and Mg concentrations considered that country rocks have low abundances of these components. Assimilation of marble country rocks can only justify Ca and Sr abundances in granite samples very close to the granite–marble interface.

Moreover, the nearest Temperino mining area is characterized by a Zn–Pb(–Ag) ore replaced by a Fe–Cu mineralization, spatially related with a batch of mafic magma (Vezzoni et al. 2016). In that model, Zn–Pb skarn predates the Fe–Cu mineralization and formed as a distal skarn having no spatial relationship with the magmatic rocks. Thus, the emplacement of mafic magma during this first stage is not required, given that deep hydrothermal fluids can be emplaced independently. Nevertheless, at Campiglia, a mafic reservoir is inferred to be active since the emplacement of the Botro ai Marmi granite (Paoli et al. 2017; Paoli 2018).

The Tuscan Magmatic Province is known notably for its peraluminous granite intrusions, similar to Botro ai Marmi granite, which has been emplaced into carbonatic rocks and the overlying tectonic units (Dini et al. 2005). These intrusions generated HT–LP metamorphism in their host rocks (e.g., Campiglia, Gavorrano, Castel di Pietra, Elba Island), but no metasomatic products comparable with those observed at Campiglia are found elsewhere. The clearest example is the Gavorrano pluton, where no metasomatic products occur even if the surrounding carbonate rocks suffered metamorphic temperatures (Rocchi et al. 2003) similar to those observed at Campiglia. Thus, the metasomatic products observed at Campiglia could not result from a simple interaction between the peraluminous granitic magma and its carbonate host rocks. Thus, the release of fluids from a mafic reservoir could account for the potassic–calcic metasomatism observed in the Campiglia system. As additional support to this interpretation, average orientation of endoskarn veins correlates with the bulged geometry of the pluton, both in the mine and in the deep borehole. Thus, the metasomatism is channeled preferentially in an NE–SW direction. These structural and metasomatic evidences could be attributed to the action of over-pressurized, mafic fluids released from a deeper source.

Furthermore, an outstanding issue is the origin of fluids able to generate the Sn–Fe(–W) deposits of Monte Valerio. In this context and according to data from the Botro ai Marmi pluton, it is possible that this distal ore deposit resulted from the mobilization of elements after the metasomatism of the main granite intrusion (Paoli et al. 2017, Paoli 2018). The occurrence of Sn–Fe(–W) deposits and of HFSE/REE minerals in skarns within hundreds of meters of the contact indicates that such fluids circulated through the aureole at temperatures similar to those responsible for contact skarn formation, suggesting a magmatic origin.

Conclusions and implications

This study shows that the origin of some fluids and metasomatic products cannot be simply explained by activities related to what can be seen at the outcrop. Hidden intrusions of different nature in a multi-pulse magmatic system can play a key role both as a source of fluids/metals as well as a trigger of chemical reactions in the host rock and in preexisting magmatic products, as well.

Detailed geochemical and mineralogical studies are fundamental to understand the single- or multi-pulse nature of a magmatic–hydrothermal system. Indeed, in a multi-pulse system, the key question is the possible existence of hidden magmatic intrusions able to generate fluids and metasomatic products. In this respect, the observations at Botro ai Marmi set the stage for detailed petrochronology studies of magmatic and metasomatic processes in a magmatic–hydrothermal system. This rather "young" system offers, indeed, a prime advantage over "old" metasomatic systems, which is the attempt to discriminate between different metasomatic events separated by time lags in the order of 10 s to 100 s ka (Paoli et al. 2017, Paoli 2018): the high-precision dating methodologies recently made available (Barboni et al. 2015; Chiaradia et al. 2013; Farina et al. 2018), when applied to systems as young as Botro ai Marmi, allow to discriminate even closely spaced events.

References

Acocella VRF, Faccenna C, Funicello R, Lazzarotto A (2000) Strike-slip faulting and pluton emplacement at Campiglia Marittima (southern Tuscany). Boll Soc Geol Ital 119:517–528

Barberi F, Innocenti F, Mazzuoli R (1967) Contributo alla conoscenza chimica-petrografica e magmatologica delle rocce intrusive, vulcaniche e filoniane del Campigliese (Toscana). Mem Soc Geol Ital 28:643–681

Barboni M, Annen C, Schoene B (2015) Evaluating the construction and evolution of upper crustal magma reservoirs with coupled U/Pb zircon geochronology and thermal modeling: a case study from the Mt. Capanne pluton (Elba, Italy). Earth Planet Sci Lett 432:436–448. https://doi.org/10.1016/j.epsl.2015.09.043

Baumgartner LP, Olsen SN (1995) A least-squares approach to mass transport calculations using the isocon method. Econ Geol 90:1261–1270. https://doi.org/10.2113/gsecongeo.90.5.1261

Bea F (1996) Residence of REE, Y, Th, and U in granites and crustal protoliths; implications for the chemistry of crustal melts. J Pet 37:521–552. https://doi.org/10.1093/petrology/37.3.521

Biagioni C, Orlandi P, Gini C, Bargellini C, Marinai V, Nannoni R (2013) Botro ai Marmi—I minerali delle miniere Maffei e Montorsi. Miniere e Miner 1:63–92

Borsi S, Ferrara G, Tongiorgi E (1967) Determinazione con il metodo K/Ar delle età delle rocce magmatiche della Toscana. Boll Soc Geol Ital 86:403–411

Caiozzi FP, Gioncada A, Sbrana A (1998) Studio SEM-EDS dei minerali figli nelle inclusioni fluide di Botro ai Marmi (Campiglia Marittima). Atti Soc tosc Sci Nat Mem 105:65–73

Chiaradia M, Schaltegger U, Spikings R, Wotzlaw JF, Ovtcharova M (2013) How accurately can we date the duration of magmatic-hydrothermal events in porphyry systems? Econ Geol 108:565–584. https://doi.org/10.2113/econgeo.108.4.565

Clarke DB (1981) The mineralogy of peraluminous granites; a review. Can Mineral 19:3–17

Dini A, Innocenti F, Rocchi S, Tonarini S, Westerman DS (2002) The magmatic evolution of the late Miocene laccolith–pluton–dyke granitic complex of Elba Island, Italy. Geol Mag 139:257–279. https://doi.org/10.1017/S0016756802006556

Dini A, Gianelli G, Puxeddu M, Ruggieri G (2005) Origin and evolution of Pliocene–Pleistocene granites from the Larderello geothermal field (Tuscan Magmatic Province, Italy). Lithos 81:1–31. https://doi.org/10.1016/j.lithos.2004.09.002

Dini A, Westerman DS, Innocenti F, Rocchi S (2008) Magma emplacement in a transfer zone: the Miocene mafic Orano dyke swarm of Elba Island, Tuscany, Italy. Geol Soc Lond 302:131–148. https://doi.org/10.1144/sp302.10

Dini A, Orlandi P, Vezzoni S (2013) Temperino e Lanzi. Le paragenesi primarie dello skarn. Rivista Mineralogica Italiana Campigliese. Miniere e Miner 1:28–39

Ducoux M, Branquet Y, Jolivet L, Arbaret L, Grasemann B, Rabillard A, Gumiaux C, Drufin S (2017) Synkinematic skarns and fluid drainage along detachments: the West Cycladic Detachment System on Serifos Island (Cyclades, Greece) and its related mineralization. Tectonophysics 695:1–26. https://doi.org/10.1016/j.tecto.2016.12.008

Durand C, Marquer D, Baumgartner L, Goncalves P, Boulvais P, Rossy M (2009) Large calcite and bulk-rock volume loss in metacarbonate xenoliths from the Quérigut massif (French Pyrenees). Contrib Miner Pet 157:749–763. https://doi.org/10.1007/s00410-008-0362-5

Einaudi MT, Meinert LD, Newberry RJ (1981) Skarn deposits. Economic geology 75th Anniversary, vol 317–391. https://doi.org/10.2113/gsecongeo.95.6.1183

Farina F, Dini A, Innocenti F, Rocchi R, Westerman DS (2010) Rapid incremental assembly of the Monte Capanne pluton (Elba Island, Tuscany) by downward stacking of magma sheets. Geol Soc Am Bull 122(9–10):1463–1479. https://doi.org/10.1130/B30112.1

Farina F, Dini A, Davies JHFL, Ovtcharova M, Greber ND, Bouvier AS, Baumgartner L, Ulianov A, Schaltegger U (2018) Zircon petrochronology reveals the timescale and mechanism of anatectic magma formation. Earth Planet Sci Lett 495:213–223. https://doi.org/10.1016/j.epsl.2018.05.021

Feldstein SN, Halliday AN, Davies GR, Hall CM (1994) Isotope and chemical microsampling: constraints on the history of an S-type rhyolite, San Vincenzo, Tuscany, Italy. Geochim et Cosmochim Acta 58(2):943–958. https://doi.org/10.1016/0016-7037(94)90517-7

Ferrara G, Petrini R, Serri G, Tonarini S (1989) Petrology and isotope-geochemistry of San Vincenzo rhyolites (Tuscany, Italy). Bull Volcanol 51:379–388. https://doi.org/10.1007/bf01056898

Franzini M, Lezzerini M, Origlia F (2010) Marbles from the Campiglia Marittima area (Tuscany, Italy). Eur J Miner 22:881–893. https://doi.org/10.1127/0935-1221/2010/0022-2056

Fulignati P (2018) Hydrothermal fluid evolution in the "Botro ai Marmi" quartz-monzonitic intrusion, Campiglia Marittima, Tuscany, Italy. Evidence from a fluid-inclusion investigation. Mineral Mag 82(5):1169–1185. https://doi.org/10.1180/mgm.2018.116

Gaspar M, Knaack C, Meinert LD, Moretti R (2008) REE in skarn systems: a LA-ICP-MS study of garnets from the Crown Jewel gold deposit. Geochim Cosmochim Acta 72:185–205. https://doi.org/10.1016/j.gca.2007.09.033

Grant JA (1986) The isocon diagram—a simple solution to Gresens' equation for metasomatic alteration. Econ Geol 81:1976–1982. https://doi.org/10.2113/gsecongeo.81.8.1976

Grant JA (2005) Isocon analysis: a brief review of the method and applications. Phys Chem Earth Parts A/B/C 30:997–1004. https://doi.org/10.1016/j.pce.2004.11.003

Gresens RL (1967) Composition-volume relationships of metasomatism. Chem Geol 2:47–65. https://doi.org/10.1016/0009-2541(67)90004-6

Griffin WL, Pearson NJ, Belousova E, Jackson SE, Van Achterbergh E, O'Reilly SY, Shee SR (2000) The Hf isotope composition of cratonic mantle: LAM–MC–ICPMS analysis of zircon megacrysts in kimberlites. Geochimica et Cosmochimica Acta 64:133–147. https://doi.org/10.1016/s0016-7037(99)00343-9

Gysi AP, Williams-Jones AE (2013) Hydrothermal mobilization of pegmatite-hosted REE and Zr at Strange Lake, Canada: a reaction path model. Geochim Cosmochim Acta 122:324–352. https://doi.org/10.1016/j.gca.2013.08.031

Gysi AP, Williams-Jones AE, Collins P (2016) Lithogeochemical vectors for hydrothermal processes in the Strange Lake Peralkaline granitic REE-Zr–Nb deposit. Econ Geol 111:1241–1276. https://doi.org/10.2113/econgeo.111.5.1241

Harlov DE, Austrheim H (2013) Metasomatism and the chemical transformation of rock: rock-mineral-fluid interaction in terrestrial and extraterrestrial environments. In: Metasomatism and the chemical transformation of rock: the role of fluids in terrestrial and extraterrestrial processes. Springer, Berlin, Heidelberg, pp 1–16. https://doi.org/10.1007/978-3-642-28394-9_1

Kwak TAP, Tan TH (1981) The importance of CaCl₂ in fluid composition trends-evidence from King Island (Dolphin) skarn deposit. Econ Geol 76:955–960

Lattanzi P, Benvenuti M, Costagliola P, Maineri C, Mascaro I, Tanelli G, Dini A, Ruggieri G (2001) Magmatic versus hydrothermal processes in the formation of raw ceramic material deposits in southern Tuscany. In: Proceedings 10th International symposium on water-rock interaction, Villasimius, 10–15 June 2001, pp 725–728. http://hdl.handle.net/2158/5600

Leoni L, Tamponi M (1991) Thermometamorphism in the Campiglia Marittima aureole (Tuscany, Italy). N Jb Miner Mh 4:145–157

López-Moro FJ (2012) EASYGRESGRANT—A Microsoft Excel spreadsheet to quantify volume changes and to perform mass-balance modeling in metasomatic systems. Comput Geosci 39:191–196. https://doi.org/10.1016/j.cageo.2011.07.014

Meinert LD, Dipple GM, Nicolescu S (2005) World skarn deposits. Economic geology 100 h Anniversary, pp 299–336. https://doi.org/10.5382/av100.11

Moore DE, Liou JG (1979) Chessboard-twinned albite from Franciscan metaconglomerates in the Diablo Range, California. Am Miner 64:329–336

Orville PM (1963) Alkali-metasomatism and feldspar. Norsk Geol Tidsskr 42:283–316

Paoli G (2018) Petrogeochemical and geochronological framework of element mobility during magmatic-metasomatic processes (Campiglia Marittima, Tuscany). Plinius 44:67–71. https://doi.org/10.19276/plinius.2018.01010

Paoli G, Rocchi S, Dini A, Vezzoni S, Schaltegger U, Ovtcharova M (2017) The plutonic-subvolcanic-volcanic connection in the long-lived Campiglia Marittima igneous system (Tucany, Italy): a zircon CA-ID-TIMS dating study. Congresso SIMP-SGI-SOGEI-AIV 2017, 387, ISSN: 2038-1719

Park C, Song Y, Chung D, Kang I-M, Khulganakhuu C, Yi K (2016) Recrystallization and hydrothermal growth of high U-Th zircon

in the Weondong deposit, Korea: Record of post-magmatic alteration. Lithos 260:268–285. https://doi.org/10.1016/j.lithos.2016.05.026

Parry W, Downey L (1982) Geochemistry of hydrothermal chlorite replacing igneous biotite. Clay Miner 30:81–90. https://doi.org/10.1346/CCMN.1982.0300201

Pinarelli L, Poli G, Santo A (1989) Geochemical characterization of recent volcanism from the Tuscan magmatic province (Central Italy): the Roccastrada and San Vincenzo centers. Per di Min 58:67–96

Pirajno F (2009) Hydrothermal processes and wall rock alteration. In: Hydrothermal processes and mineral systems. Springer, Dordrecht, pp 73–164 https://doi.org/10.1007/978-1-4020-8613-7_2

Pirajno F (2013) Effects of metasomatism on mineral systems and their host rocks: alkali metasomatism, skarns, greisens, tourmalinites, rodingites, black-wall alteration and listvenites. In: Metasomatism and the chemical transformation of rock: the role of fluids in terrestrial and extraterrestrial processes. Springer, Berlin, Heidelberg, pp 203–251. https://doi.org/10.1007/978-3-642-28394-9_7

Plümper O, Putnis A (2009) The complex hydrothermal history of granitic rocks: multiple feldspar replacement reactions under subsolidus conditions. J Pet 50:967–987. https://doi.org/10.1093/petrology/egp028

Poli G, Peccerillo A (2016) The Upper Miocene magmatism of the Island of Elba (Central Italy): compositional characteristics, petrogenesis and implications for the origin of the Tuscany Magmatic Province. Mineral Petrol 110:421–445. https://doi.org/10.1007/s00710-016-0426-6

Poli G, Manetti P, Tommasini S (1989) A petrological review on Miocene-Pliocene intrusive rocks from Southern Tuscany and Tyrrhenian Sea (Italy). Period di Mineral 58:109–126

Ridolfi F, Renzulli A, Perugini D, Cesare B, Braga R, Del Moro S (2009) Unravelling the complex interaction between mantle and crustal magmas encoded in the lavas of San Vincenzo (Tuscany, Italy). Part II: Geochemical overview and modelling. Lithos 244:233–249. https://doi.org/10.1016/j.lithos.2015.11.002

Rocchi S, Dini A, Mazzarini F, Poli G (2003) Campiglia Marittima and Gavorrano intrusive magmatism. Period di Mineral 72:127–132

Rodolico F (1945) Ragguagli sul granito del Campigliese. Atti della Soc Toscana di Sci Nat 73:62–74

Rossetti F, Faccenna C, Acocella V, Funicello R, Jolivt L, Salvini F (2000) Pluton emplacement in the northern Tyrrenian area, Italy. Geol Soc Lond 174:55–77. https://doi.org/10.1144/GSL.SP.1999.174.01.04

Samim (1983) Note di commento ai sondaggi di Monte Spinosa. Internal Report. http://www.neogeo.unisi.it/dbgmnew/ricerca.asp?act=see&id=11890

Schaltegger U (2007) Hydrothermal zircon. Elements 3:78–79. https://doi.org/10.2113/gselements.3.1.51

Seedorff E, Dilles JH, Proffett JM, Einaudi MT, Zurcher L, Stavast WJA, Johnson DA, Barton MD (2005) Porphyry deposits: characteristics and origin of hypogene features. Econ Geol 100:251–298

Sillitoe RH (2010) Porphyry copper systems. Econ Geol 105:3–41. https://doi.org/10.2113/gsecongeo.105.1.3

Sun SS, McDonough WF (1989) Chemical and isotopic systematics of oceanic basalts: implications for mantle composition and processes. In Magmatism in the Ocean Basins (eds A. D. Saunders and M. J. Norry). Geol Soc Lond 42:315–345. https://doi.org/10.1144/GSL.SP.1989.042.01.19

Vezzoni S, Dini A, Rocchi S (2016) Reverse telescoping in a distal skarn system (Campiglia Marittima, Italy). Ore Geol Rev 77:176–193. https://doi.org/10.1016/j.oregeorev.2016.03.001

Vezzoni S, Rocchi S, Dini A (2018) Lateral extrusion of a thermally weakened pluton overburden (Campiglia Marittima, Tuscany). Int J Earth Sci (Geol Rundsch) 107:1343. https://doi.org/10.1007/s00531-017-1539-9

Villaseca C, Pérez-Soba C, Merino E, Orejana D, López-García JA, Billstrom K (2012) Contrasted crustal sources for peraluminous granites of the segmented Montes de Toledo Batholith (Iberian Variscan Belt). J Geosci. https://doi.org/10.3190/jgeosci.035

Whitney DL, Evans BW (2010) Abbreviations for names of rock-forming minerals. Am Miner 95:185–187

Yang WB, Niu HC, Shan Q, Luo Y, Yu XY (2009) Ore-forming mechanism of the Baerzhe super-large rare and rare earth elements deposit. Acta Pet Sin 25:2924–2932